Received: 16 March 2023 | Revised: 23 February 2024 | Accepted: 29 February 2024
DOI: 10.1002/esp.5819

RESEARCH ARTICLE

ESPL WILEY

The grain size of sediments delivered to steep debris-flow prone channels prior to and following wildfire

Alexander B. Neely[1,2,3] | **Seulgi Moon**[1] | **Roman A. DiBiase**[2,4] | **Leonard S. Sklar**[5] | **Marina O. Argueta**[1]

[1]Department of Earth, Planetary, and Space Sciences, University of California, Los Angeles, Los Angeles, California, USA

[2]Department of Geosciences, Pennsylvania State University, University Park, Pennsylvania, USA

[3]Department of Geosciences, University of Tübingen, Tübingen, Germany

[4]Earth and Environmental Systems Institute, Pennsylvania State University, University Park, Pennsylvania, USA

[5]School of Environmental Science, Simon Fraser University, Burnaby, British Columbia, Canada

Correspondence
Alexander B. Neely, Department of Earth, Planetary, and Space Sciences, University of California, Los Angeles, Los Angeles, CA 90095-1567, USA.
Email: abngeology@gmail.com; alexander-banks.neely@uni-tuebingen.de

Funding information
National Science Foundation, Grant/Award Numbers: EAR-1945431, EAR-2012073, EAR-1848321, EAR-1608014

Abstract

Debris flows are powered by sediment supplied from steep hillslopes where soils are often patchy and interrupted by bare-bedrock cliffs. The role of patchy soils and cliffs in supplying sediment to channels remains unclear, particularly surrounding wildfire disturbances that heighten debris-flow hazards by increasing sediment supply to channels. Here, we examine how variation in soil cover on hillslopes affects sediment sizes in channels surrounding the 2020 El Dorado wildfire, which burned debris-flow prone slopes in the San Bernardino Mountains, California. We focus on six headwater catchments (<0.1 km^2) where hillslope sources ranged from a continuous soil mantle to 95% bare-bedrock cliffs. At each site, we measured sediment grain size distributions at the same channel locations before and immediately following the wildfire. We compared results to a mixing model that accounts for three distinct hillslope sediment sources distinguished by local slope thresholds. We find that channel sediment in fully soil-mantled catchments reflects hillslope soils ($D_{50} = 0.1$–0.2 cm) both before and after the wildfire. In steeper catchments with cliffs, channel sediment is consistently coarse prior to fire ($D_{50} = 6$–32 cm) and reflects bedrock fracture spacing, despite cliffs representing anywhere from 5% to 95% of the sediment source area. Following the fire, channel sediment size reduces most (5- to 20-fold) in catchments where hillslope sources are predominantly soil covered but with patches of cliffs. The abrupt fining of channel sediment is thought to facilitate postfire debris-flow initiation, and our results imply that this effect is greatest where bare-bedrock cliffs are present but not dominant. A patchwork of bare-bedrock cliffs is common in steeplands where hillslopes respond to channel incision by landsliding. We show how local slope thresholds applied to such terrain aid in estimating sediment supply conditions before two destructive debris flows that eventually nucleated in these study catchments in 2022.

KEYWORDS
debris flow, grain size, hazard, hillslope, mountain, mudflow, sediment, steep, wildfire

1 | INTRODUCTION

In steep landscapes, sediment delivery to channels often includes a combination of weathered material from soil-mantled hillslopes and coarser debris from landslides and bare-bedrock cliffs (Roda-Boluda et al., 2018; Sklar et al., 2020). Wildfires can alter the partitioning of hillslope sediment delivery from soil-mantled and bedrock hillslope sources because of changes in vegetation cover or surface material properties, and rapid fining of channel bed material has been invoked as a potential precursor to destructive postfire debris flows (Florsheim et al., 1991; Palucis et al., 2021). The resulting sediment mixture delivered from hillslopes to steep channels influences debris-flow initiation criteria, flow mechanics and inundation patterns throughout downstream environments (Alessio et al., 2021; Huebl & Kaitna, 2021; Kostynick et al., 2022; McGuire et al., 2017; Meyer & Wells, 1997). Predicting the size distribution of sediment in any channel is a fundamental challenge (Sklar et al., 2017), and few studies contextualise sediment grain sizes in channels with wildfire dynamics (Florsheim et al., 1991; Nyman et al., 2020; Wall et al., 2023).

While empirically derived rainfall intensity-duration thresholds are commonly used to forecast the occurrence of postfire debris flows (e.g. Cannon et al., 2008; Staley et al., 2017), the source and amount of sediment incorporated into debris flows varies widely between events (Guilinger et al., 2020; McGuire et al., 2016; Morell et al., 2021; Schmidt et al., 2011; Staley et al., 2014; Wall et al., 2023). The total postfire sediment yield is usually a combination of sediment eroded from hillslopes following fire and coarser colluvial sediment that was presumably stored in the channel network prior to fire (Guilinger et al., 2020; Morell et al., 2021). The response of wildfire dynamics to future climates is uncertain (Keeley & Syphard, 2016), but in general, postfire debris-flow hazards are expected to occur more frequently and with higher severity at urban-wildlife interfaces (Kean & Staley, 2021). Postfire sediment delivered to larger rivers downstream can also have adverse effects on water quality and ecosystem function (Murphy et al., 2019; Writer & Murphy, 2012). The grain size and amount of sediment released from hillslopes and headwater channel sediment sources remain largely unconstrained in this context, particularly in regions that have not experienced historic burns because of fire suppression tactics or in regions where fire regimes shift in future climate scenarios (Abatzoglou et al., 2021; Steel et al., 2015).

The amount of sediment delivered from steep hillslopes to channels can increase by 10 to 100 times relative to background rates following the wildfire (East et al., 2021; Jackson & Roering, 2009; Lamb et al., 2011; Roering & Gerber, 2005). Of particular importance is the potential for dry ravel transport of fine-grained material following the incineration of vegetation on steep hillslopes (DiBiase & Lamb, 2013; Florsheim et al., 1991), soil erosion by rilling during storms (Alessio et al., 2021; Hyde et al., 2014; McGuire et al., 2017; Rengers et al., 2021), sediment production by fire-spallation on exposed bedrock (De Graff & Gallegos, 2012; Sarro et al., 2021), and prefire colluvial sediment stored within channel valleys (Morell et al., 2021; Nyman et al., 2020; Santi et al., 2008). Postfire dry ravel transport is characteristic of rapidly eroding transverse ranges of southern California (DiBiase & Lamb, 2020), where hillslopes are a patchwork of bare-bedrock cliffs and vegetated hillsides perched near slope-stability thresholds (Binnie et al., 2007; DiBiase et al., 2023). However, the magnitude and importance of dry ravel processes are highly variable across mountain landscapes in the western United States (Alessio et al., 2021; East et al., 2021), possibly because of differences in bedrock lithology, soil particle size and sorting, or subtle differences in topographic gradient with respect to threshold stability angles of loose sediment (DiBiase & Lamb, 2020; Lamb et al., 2013).

Regardless of the specific hillslope sediment transport process that moves sediment into channels, resurfacing previously coarse-grained channels with fine-grained sediments reduces thresholds for debris-flow initiation (Cannon et al., 2008; Florsheim et al., 2017; Meyer & Wells, 1997; Nyman et al., 2020; Palucis et al., 2021). These temporal changes in surface sediment grain size distribution also imply that wildfire and vegetation dynamics impart size-selective controls on hillslope sediment transport processes (Roth et al., 2020), which may have broad importance for the transfer of sediment from hillslopes to headwater channels. However, constraining sediment dynamics surrounding fires requires timely sediment grain size surveys in channels before and after the fires (Florsheim et al., 1991), characterisation of the grain size distribution of sediment derived from distinct hillslope sediment sources (Roda-Boluda et al., 2018; Sklar et al., 2017), and description of the impact of fire on distinct hillslope sediment sources (Larsen et al., 2006).

The size distribution of sediments delivered from hillslopes to channels is a complicated product of initial bedrock properties, rock weathering processes, and the duration of weathering near the land surface (e.g. Sklar et al., 2017), but broad differences in the grain size of sediment supply can be distinguished between soil-mantled landscapes and steeper landslide-prone landscapes with exposed bedrock cliffs (Attal et al., 2015; Lukens et al., 2016; Neely & DiBiase, 2020; Roda-Boluda et al., 2018). Sediments derived from bare-bedrock cliffs and landslides typically reflect inherited rock properties such as the spacing of fractures, whereas soil-derived sediment is fined by weathering, which depends on climate, biota, and soil age (Neely & DiBiase, 2020; Román-Sánchez et al., 2021; Terweh et al., 2021). Importantly, the broad distinction between bare-bedrock cliffs and soil-mantled hillslopes can be mapped across landscapes either directly with high-resolution imagery (Neely et al., 2019) or with topographic proxies derived from airborne lidar surveys (DiBiase et al., 2012; Milodowski et al., 2015). Here, we use topography derived from airborne lidar data to classify hillslope soil cover conditions. Then, we link these topographic and surface cover classifications to spatial patterns of sediment grain size throughout debris-flow source regions before and after the wildfire.

Our study design examines sediment grain size distributions in headwater channel networks where contributing hillslopes exhibit a variable patchwork of soil cover and bare-bedrock cliff exposure, before (2018) and immediately after the 2020 El Dorado Fire, which burned steep terrain across Yucaipa Ridge in the San Bernardino Mountains, California. We focus our analysis on six small (<1 km^2) watersheds that have hillslope sources ranging from fully soil-mantled to complete bare-bedrock cliff exposure. We evaluate how the grain size of sediment changed in each channel following the wildfire. Our 2018 observations constrain the prefire hillslope and headwater channel conditions, and our 2020 observations constrain the immediate postfire hillslope and headwater channel conditions, prior to precipitation events that could trigger postfire debris flows. Additionally, we quantified the size distribution of sediments directly on three hillslope sediment source types that vary in their local topographic slope: low-sloping soil-mantled hillslopes, steeper dry ravel-prone hillslopes, and bare-bedrock hillslope sediment sources. We compare modelled grain size distributions of postfire sediment supply estimated from an area-weighted mixture of these three distinct sediment sources to (1) observe changes in sediment size in channels immediately following the fire and (2) qualitative observations of postfire debris flows that occurred in September 2022 within two of the studied watersheds.

Our goals are to (1) present timely observational data that describe changes in surface sediment grain sizes from headwater channels prior to and following the wildfire; (2) contextualise patterns in headwater channel sediment grain size with analysis of different hillslope sediment sources that can be extracted with topographic metrics; and (3) explore a framework that uses the areal extent of hillslope sediment sources and a representative grain size distribution of their sediment supply to estimate the size distribution of sediment available for postfire debris flows.

2 | STUDY AREA

2.1 | Geologic and climatic setting in the San Bernardino Mountains, southern California

Our analysis focusses on Yucaipa Ridge, which is a <10-km wide, fault-bounded block along the southwestern edge of the San Bernardino Mountains, California, USA, with 1–2 km of topographic relief. Yucaipa Ridge is an ideal site to study connections among topography, weathering, wildfire and sediment supply to debris flows because of its geologic setting and preexisting high-resolution topographic and field datasets. Sites across Yucaipa Ridge are underlain by highly fractured gneissic and granitic rock of Cretaceous and older ages and bounded to the north and south by segments of the San Andreas Fault (Allen, 1957; Bortugno & Spittler, 1986). Transpression on high-angle faults produces consistently rapid rates of rock uplift and erosion in the region. An estimated 3–6 km of exhumation occurred across the Yucaipa Ridge block in the past ~1.5 million years (Spotila et al., 2001). Relief, topographic slope and exposure of bare-bedrock cliffs vary within the mountain range but generally track differences in ^{10}Be-derived erosion rates that range from 0.2 to 2.7 m kyr^{-1} (Argueta et al., 2023; Binnie et al., 2007).

Yucaipa Ridge experiences a semi-arid climate with a mean annual rainfall of approximately 100 cm yr^{-1} (Minnich et al., 1995). Mean annual precipitation varies minimally (<10%) across the watersheds examined (1991–2020 PRISM Climate Group, Oregon State University, https://prism.oregonstate.edu, data created Nov. 2021, accessed 14 Dec 2022). Vegetation is characterised by mixed conifer forests that occupy elevations between 1400 and 2600 m and include ponderosa pine, Jeffrey pine, and white fir (Minnich et al., 1995). Chaparral dominates below elevations of 1400 m, with manzanita, chamise, heteromeles, yucca and scrub oak (Minnich, 1988). Most precipitation is delivered during winter storms and summer convective thunderstorms (Minnich et al., 1995). Climate records from 1956 to 1980 indicate that between 5% and 60% of total winter storm precipitation was delivered as snowfall across study site elevations (Minnich, 1986). The combination of rapid rock uplift rates, high topographic relief, and high rainfall intensities produces debris flows. Since 1955, at least 11 historic debris flows have been noted on the north side of Yucaipa Ridge, east of the study region. These events were unrelated to wildfire and primarily associated with summer convective thunderstorms (Morton et al., 2008).

Between 5 September and 16 November 2020, the El Dorado Fire burned ~93 km^2 of the San Bernardino Mountains, including the steep terrain of Yucaipa Ridge (Figure 1). The fire was triggered by a malfunctioning pyrotechnical device at a gender reveal party held at nearby El Dorado Park (USDA Forest Service BAER, 2020). Steep terrain within Yucaipa Ridge had not burned since fire suppression tactics were employed across the southwestern United States in the early 20th century (Minnich, 1988, https://frap.fire.ca.gov/mapping/gis-data/). Since this time period, the density of trees had increased by ~80% for all trees exceeding 12-cm diameter at breast height, with 3- to 10-fold increases in the smallest fraction of trees between 12- and 66-cm diameter at breast height (Minnich et al., 1995). High fuel loads were present prior to the fire. Around 71% of the area within the El Dorado Fire perimeter experienced moderate to high soil burn severities, and predictions for postfire debris-flow hazards were rated as extremely likely (USDA Forest Service BAER, 2020).

2.2 | Theoretical framework

In the steepest mountain settings, hillslope gradients are thought to directly reflect slope stability limits and adjust to local channel incision by landsliding (Binnie et al., 2007; Schmidt & Montgomery, 1995). However, landsliding removes soil cover and vegetation and exposes underlying bedrock (Heimsath et al., 2012). The underlying bedrock commonly has a different slope stability limit than soil material that was previously detached from bedrock. Hillslope gradients thus vary spatially depending on the exposure of underlying bare bedrock or the presence of vegetation (Moore et al., 2009; Neely et al., 2019; Schmidt et al., 2001). When examining morphodynamics of steep hillslopes, a problem emerges to describe the relative abundance of soil-mantled and bare-bedrock slopes and the threshold slopes of these hillslope types (DiBiase et al., 2023).

Sediment transport across the resulting mixture of soil-mantled and bare-bedrock hillslope types is complex. If local slopes exceed stability angles for loose soil, soil transport can occur across long distances that are not easily described by an effective length scale, and soil transport fluxes are dependent on clast-specific travel paths across the topographic surface (Foufoula-Georgiou et al., 2010; Gabet & Mendoza, 2012). Moreover, soil thickness varies spatially as a consequence of variations in local supply of weathered bedrock from below or accumulation of colluvium that is supplied from upslope locations where loose soil is unstable, such as bedrock cliffs. To accommodate non-local effects, steep hillslope sediment transport models employ particle-based probabilistic approaches that simulate interactions among local topography, particle size, friction and particle acceleration along a downslope trajectory (DiBiase et al., 2017; Li & Lan, 2015; Roth et al., 2020). These approaches can be computationally expensive and difficult to connect to geologic timescales that are needed to develop hillslope relief and soil thicknesses.

Our analysis does not attempt to model the downslope transport of sediment across the patchwork of hillslope types exposed in study sites on Yucaipa Ridge or the evolution of the patchwork of bare-bedrock and soil-mantled hillslopes over geologic timescales. Instead, we focus on two snapshots of the landscape in geologic time surrounding the El Dorado Fire. We focus on (1) the relative abundance of hillslope sediment source types, (2) the role of fire in removing hillslope vegetation, and (3) sediment grain size characteristics of deposits that resulted from hillslope sediment transport processes before and after the fire.

We first define two threshold slopes that are then used to classify three hillslope sediment source types: bare-bedrock hillslopes, steeper dry-ravel prone soil-mantled hillslopes and lower-gradient soil-

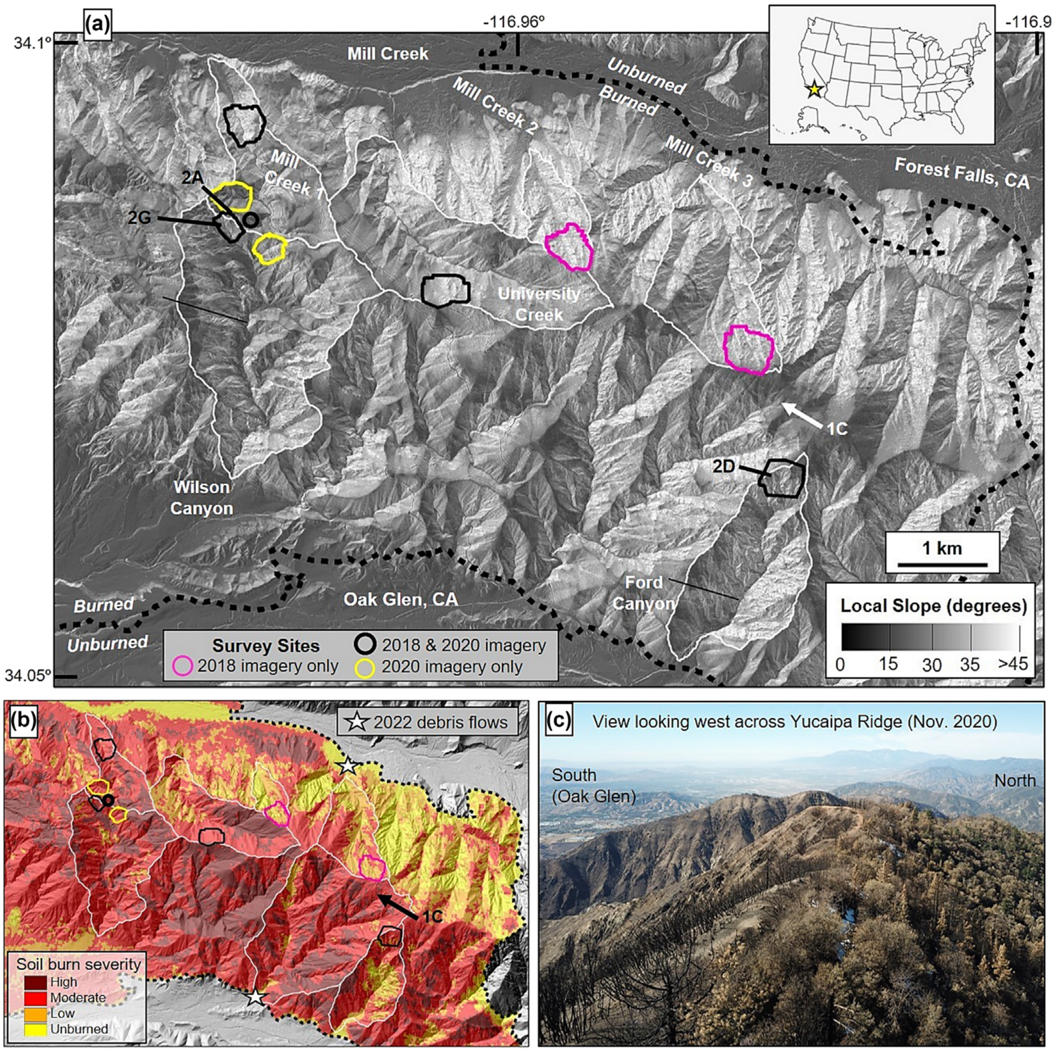

FIGURE 1 (a) Map of local slope across the burned region on Yucaipa Ridge, California measured from a 1-m resolution digital elevation model (U.S. Geological Survey, 2020). Thick lines outline the extent of photo surveys prior to and immediately following the fire (black), only prior to the fire (pink), and only following the fire (yellow). Watersheds referred to in the main text are outlined in thin white lines, and the burn perimeter from the 2020 El Dorado wildfire is marked with a black-dashed line (USDA Forest Service, 2020). (b) Soil burn severity classifications from burned area emergency response (BAER) team (USDA Forest Service, 2020). Stars indicate locations of destructive debris flows that occurred in fall 2022. (c) Postfire photograph of Yucaipa ridge looking west from Ford Canyon peak (Cedar Mountain), with viewpoint indicated in Figure 1.

mantled hillslopes. Bare bedrock is defined as in-place rock, and soil is collectively defined as all particles on hillslopes that have been detached from bedrock (i.e., mobile regolith or colluvial soil). Channel deposits were distinguished by the presence of banks, locally concave-up topography and downslope orientation of clasts in imagery. First, an upper threshold slope distinguishes between steeper bare-bedrock hillslopes where no loose soil can accumulate and lower slopes where colluvial soils are stable in the presence of vegetation. These bare-bedrock slopes are referred to as ‘cliffs’ and reflect properties of the bedrock fracture network that support slopes that are steeper than soils supported by vegetation cohesion (Moore et al., 2009; Schmidt et al., 2001). A second, lower threshold slope distinguishes between steeper, dry ravel-prone hillslopes where soils are only conditionally stable (in the presence of vegetation) and soil-mantled hillslopes where soils are stable even in the absence of vegetation cover. Vegetation increases the threshold slope angle of colluvial soils by rooting or forming coalescing debris wedges behind plants or downed logs (Adams et al., 2023; DiBiase & Lamb, 2013; Lamb et al., 2013; Schmidt et al., 2001). If vegetation is removed during events such as wildfires, soil is destabilised from slopes that are between these lower and upper slope thresholds, leading to dry ravel sediment transport (DiBiase & Lamb, 2020; Jackson & Roering, 2009). Soil on slopes lower than the second threshold slope is presumed to be stable during dry conditions over postfire timescales of a few years, even after wildfire removes vegetation; however, these slopes can contribute sediment to channels during overland flow events that erode soil.

3 | METHODS

3.1 | Hillslope sediment source mapping

We defined three distinct hillslope sediment source types at Yucaipa Ridge, based primarily on local topographic slope and hillslope response to wildfire: (1) low-sloping, soil-mantled hillslopes where dry sediment is stable following the wildfire (Figure 2c); (2) steeper soil-mantled hillslopes where sediment moves following the burning of surface vegetation (dry-ravel hillslopes); and (3) bare-bedrock cliffs, where sediment is not stable even during unburned conditions (Figure 3). The distinction between each of these three hillslope units was made using empirically derived thresholds in local topographic

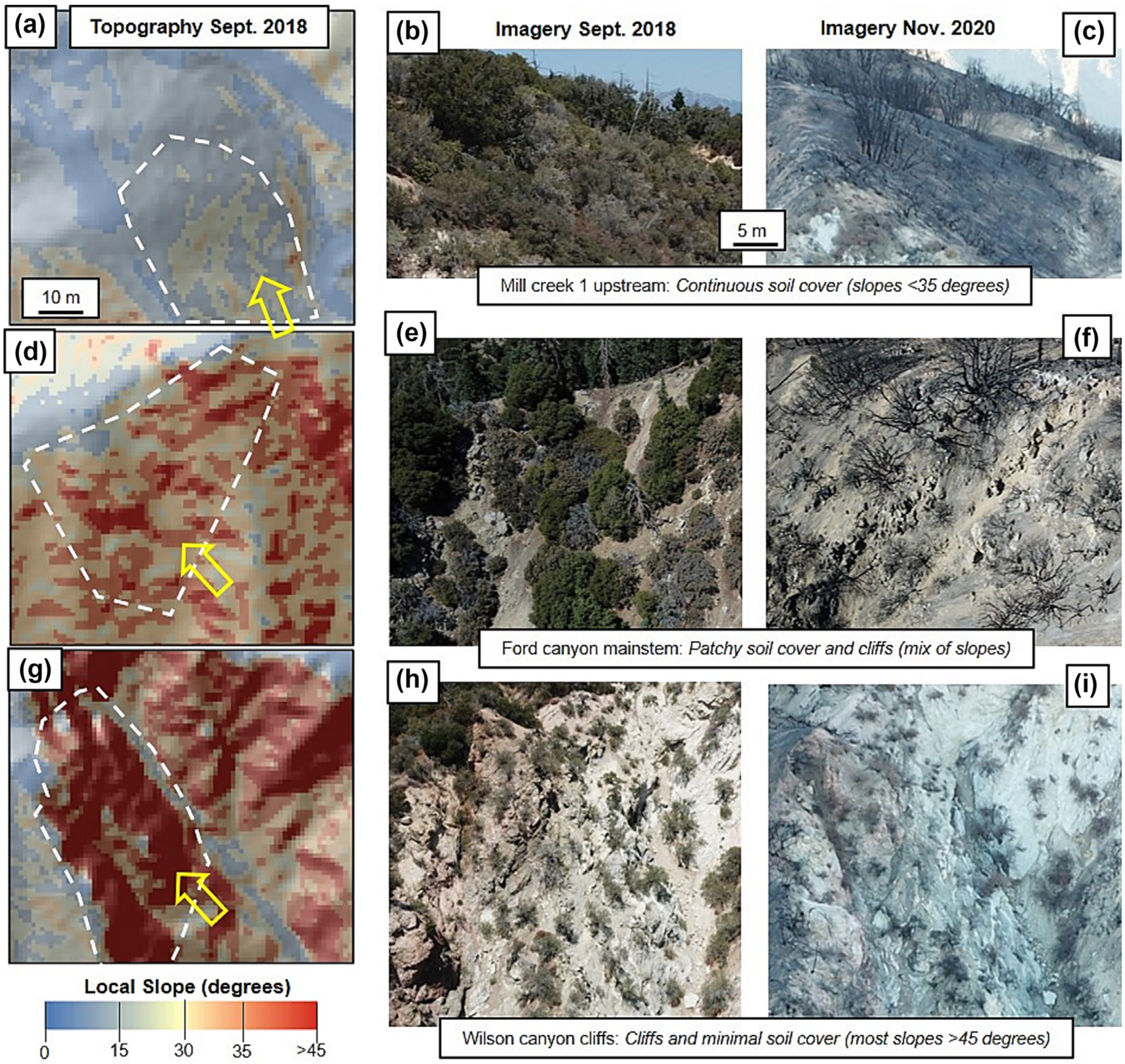

FIGURE 2 (a, d, g) Example of headwater channel sites with airborne-lidar-derived topographic data (U.S. Geological Survey, 2020), 10-m scale bar. Open yellow arrow indicates view direction for repeat photographs from white-dashed regions (b, e, h) before and (c, f, i) after the 2020 El Dorado fire (~5-m scale bar), (a–c) hillslopes with continuous soil cover; (d–f) hillslopes with a patchwork of soil-cover and bare-bedrock cliff exposure; (g–i) hillslopes with minimal soil cover. The locations of headwater sites are shown in Figure 1.

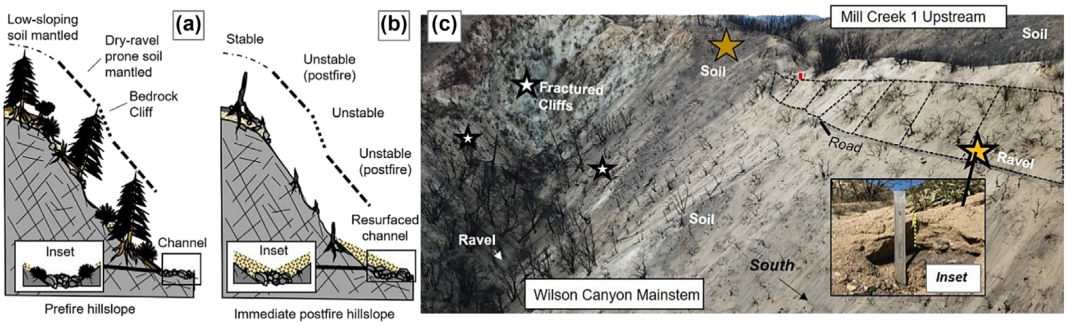

FIGURE 3 (a, b) Schematic diagram showing the partitioning of hillslope sediment sources based on local slope, stability of dry sediment, and postfire response. Inset shows resurfacing of channel by postfire sediment. (c) November 2020 photograph of Wilson Canyon watershed showing three different hillslope sediment source types in close proximity (brown star, soil; yellow star, ravel; white star, fractured cliffs). Note the undisturbed darker ash layer mantling the gentlest soil covered hillslopes. Dashed black lines show positions of 10-m-wide dry ravel deposits (inset) measured along an unnamed dirt road below the Yucaipa Ridge Truck Trail. A small red line shows the height of a curious geomorphologist (~1.85 m).

slope (Section 3.1.2), calibrated with observations from high-resolution uncrewed aerial vehicle (UAV) imagery surveys, as described below.

3.1.1 | Bedrock mapping from UAV surveys

We defined surface cover on hillslopes as soil-mantled or exposed bare bedrock using scaled and georeferenced 1-cm pixel^{-1} resolution orthomosaic images of the ground surface following Neely et al. (2019). All aerial imagery was collected using a DJI Mavic Pro, and orthomosaics were rendered from 3D structure-from-motion (SfM) photogrammetry models constructed using Agisoft Metashape Professional Version 1.8.5 (Neely et al., 2023a, 2023b). The resulting models were georeferenced to airborne lidar point clouds collected prior to fire in 2013 using iterative-closest-point alignment as described by Neely et al. (2019) (Table S1) (U.S. Geological Survey, 2020). The 75th percentile of cloud-to-cloud (M3C2) distances between lidar and SfM-derived point clouds were less than ~3 m over spatial scales of >100 m (Lague et al., 2013). No vegetation filtering was performed on 3D SfM-derived point clouds, so cloud-to-cloud distances include differences in point density and vegetation reconstruction between both point clouds. The 75th percentile cloud-to-cloud distances are consistently less than mean prefire vegetation heights, which were calculated as the mean cloud-to-mesh distance between vegetation classified lidar points and a 2.5D meshed surface constructed between bare-earth classified lidar points (Table S1). Calculated cloud-to-cloud distances likely represent maximum misfits for a given percentile, particularly in postfire cases where significant changes in vegetation height occurred. Horizontal alignment between repeat UAV orthoimages was assessed by tracing the edges of road features on 2018 and 2020 imagery, where present, and calculating distances between road traces discretised at 1-cm point spacings. Mean distances between road edges are 1.3 m (±0.9, 1σ), with a maximum offset of 3.0 m. Road features used for horizontal accuracy assessment were located near the edges of orthoimages where model distortion is typically highest and offsets also likely represent a maximum estimate.

Bare bedrock was mapped visually as patches of intact fractured rock outcrops that typically exceeded 9 m^2, a 3 × 3 pixel neighbourhood on a 1-m resolution digital elevation model (supplementary datasets S1, S3). Soil-mantled hillsides collectively include loose sediment, vegetated hillsides and grussified saprolite where fresh bedrock fracture surfaces are no longer visible. Distortions and interpolation artifacts within UAV-derived orthoimages are typically restricted to areas that are near the edges of surveys and were identified by comparing repeat UAV orthoimages where available and spatial patterns of M3C2 residuals. Distorted regions near the edges of surveys were not included in bedrock and soil cover mapping, and the original oblique and nadir imagery was used to better interpret poorly resolved or distorted regions elsewhere in the orthoimages. Overall alignment mismatch (<1–3 m) between aerial lidar topography and orthoimages can also affect topographic-based proxies of surface cover (Section 3.1.2) by classification errors near the edges of cliff features. This effect reduces topographic differences between bare bedrock and soil covered hillslope classifications but is minimised if cliff features extend over areas significantly larger than alignment mismatches (tens to hundreds of meters).

3.1.2 | Topographic analysis and hillslope sediment source partitioning

Within the broad class of soil-mantled hillslopes, we distinguish between low-sloping soil-mantled and steep dry ravel-prone hillslopes using a threshold slope of 35°. A threshold slope of 35° (1σ error = ±0.5°) was determined by fitting planes to the surface of 20 individual meter-scale dry ravel deposits resolved in cm-scale resolution 3D point clouds described in Section 3.1.1 (Thiele et al., 2017) (example deposits in Figures 3c and S1A). We assumed that each dry ravel deposit represents the angle of repose for unvegetated hillslope soils. Hillslopes below this angle do not deliver sediment by dry ravel following the wildfire and are classified as low-sloping, soil-mantled hillslopes ($A_{S<35}$), whereas hillslopes above this angle are unstable in the absence of vegetation (Figure 3).

To further distinguish between steep dry ravel-prone soil-mantled slopes and bare-bedrock slopes, we employed a calibration between local topographic slope and bare-bedrock exposure mapped from aerial imagery (Section 3.1.1). This calibration upscales our local surface cover mapping of bare-bedrock exposure across 10^4–10^5 m^2 extents (Figure 1 and Table 1) to the entire extent of aerial lidar surveys, which cover the full burn area of 93 km^2 across Yucaipa Ridge. Local slope was measured over a 3 × 3-m^2 window on a 1-m resolution bare-earth digital elevation model derived from a 2013 airborne lidar survey (U.S. Geological Survey, 2020), and we calibrated a metric of rock exposure using a slope threshold of 45° (DiBiase et al., 2012):

$$F_{\mathrm{bedrock\_M}} = K F_{S>45} \tag{1}$$

where $F_{\mathrm{bedrock\_M}}$ is the fractional area of bare bedrock exposed mapped in a region (Section 3.1.1), and $F_{S>45}$ is the fractional area with local slopes greater than 45° in a region. K is a calibration coefficient of order 1 fit by fixed linear regression through the origin (DiBiase et al., 2012).

We found a best-fit K of 0.97±0.30 ($R^2 = 0.84$) across 12 individual calibration sites where bare-bedrock exposure was mapped (Table 1 and Figure 4c). We assume $K = 1$, which permits direct mapping between hillslope locations with local gradients steeper than 45° ($A_{S>45}$) and locations with bedrock exposure (A_{bedrock}). A linear relationship between $A_{S>45}$ and A_{bedrock} with $K = 1$ is within the error of the best-fit regression. Scatter between individual sites is considerable and may reflect differences in bedrock cliff morphology or vegetation filtering differences within the digital elevation model (Milodowski et al., 2015).

Overall, we aim to determine the grain size distribution of sediment delivered from a mix of hillslope sediment sources to headwater channels following the wildfire. According to our conceptual model, postfire sediment delivery to channels in the Yucaipa Ridge region comes from one or more of the three hillslope sediment source classifications (Section 3.1). We calculated a modified hillslope source area, A_{source}, for each watershed analysed, which includes the effect of soil burn severity:

$$A_{\mathrm{source}} = A_{\mathrm{bedrock}} + A_{\mathrm{burned}}, \tag{2}$$

where A_{burned} indicates the extent of lower-sloping soil-mantled hillslopes and steeper dry-ravel hillslopes with moderate to high soil

TABLE 1 Topography, bare-bedrock exposure, and soil-burn-severity of hillslopes in survey sites.

						Watershed characteristics[c]					Hillslope sediment source fractions[d]		
Site name	Total area (m^2)	Imagery date[a] Year	Mean slope (°)	Mean elev. (m)	$A_{channel}$[b] (m^2)	Aspect	$F_{bedrock\_M}$	F_{burned}	A_{burned} (m^2)	A_{source} (m^2)	$F_{bedrock}$	F_{ravel}	F_{soil}
Mill creek 1 tributary	56,413	2020	29.9	1571	-	E	0.020	0.98	54,138	54,321	0.003	0.199	0.798
Mill creek 1 downstream	6,792	2018; 2020	41.5	1400	280	W	0.057	0.61	3,913	5,502	0.289	0.574	0.138
Mill creek 1 upstream	43,581	2018; 2020	25.1	1590	1,890	E	0.002	1.00	43,493	43,581	0.006	0.121	0.873
Mill creek 2	112,779	2018	37.0	2357	-	N	0.092	0.19	19,371	33,817	0.427	0.267	0.305
Mill creek 3	88,646	2018	43.6	2114	-	N	0.230	0.16	10,589	40,975	0.742	0.196	0.062
University creek	68,282	2018	36.7	1898	-	N	0.047	1.00	65,073	68,282	0.090	0.510	0.400
Wilson canyon tributary 1	4,770	2020	39.9	1572	-	W	0.076	1.00	4,418	4,770	0.140	0.723	0.137
Wilson canyon tributary 2	5,353	2020	39.6	1530	-	W	0.160	1.00	4,496	5,353	0.153	0.648	0.199
Wilson canyon mainstem	3,703	2018; 2020	44.4	1584	180	S	0.532	0.49	859	2,482	0.654	0.281	0.065
Wilson canyon cliffs	664	2018; 2020	48.4	1580	50	E	0.948	0.57	20	426	0.906	0.068	0.026
Ford canyon mainstem	17,740	2018; 2020	43.5	2345	650	S	0.110	0.71	11,215	17,338	0.353	0.555	0.092
Ford canyon tributary	1,045	2018; 2020	49.8	2314	170	S	0.439	0.14	80	728	0.890	0.099	0.011

[a] The six sites with repeat channel surveys from both 2018 and 2020 have two grain size distribution measurements and corresponding prefire and postfire comparisons (Table 2 and Figure 7).

[b] Only measured for sites with repeat channel surveys in both 2018 and 2020.

[c] Aspect refers to the flow direction of the main channel averaged in map directions to ±45°. $F_{bedrock\_M}$ is fraction of watershed area with bedrock exposure mapped from orthoimagery (Figure 4c). A_{burned} is the area of hillslopes within the watershed area with moderate and high soil burn severities and local slope less than 45°. A_{source} is the area within the watershed area containing burned hillslopes with local slope less than 45° and all slopes exceeding 45°. F_{burned} is the fraction of burned slopes that are not classified as exposed bare bedrock ($A_{burned}/(A_{total} - [F_{bedrock} \cdot A_{total}])$).

[d] Fraction of A_{source} corresponding to each hillslope sediment source type, classified by local topographic slope and soil burn severity, representing hillslope contributions to postfire sediment supply.

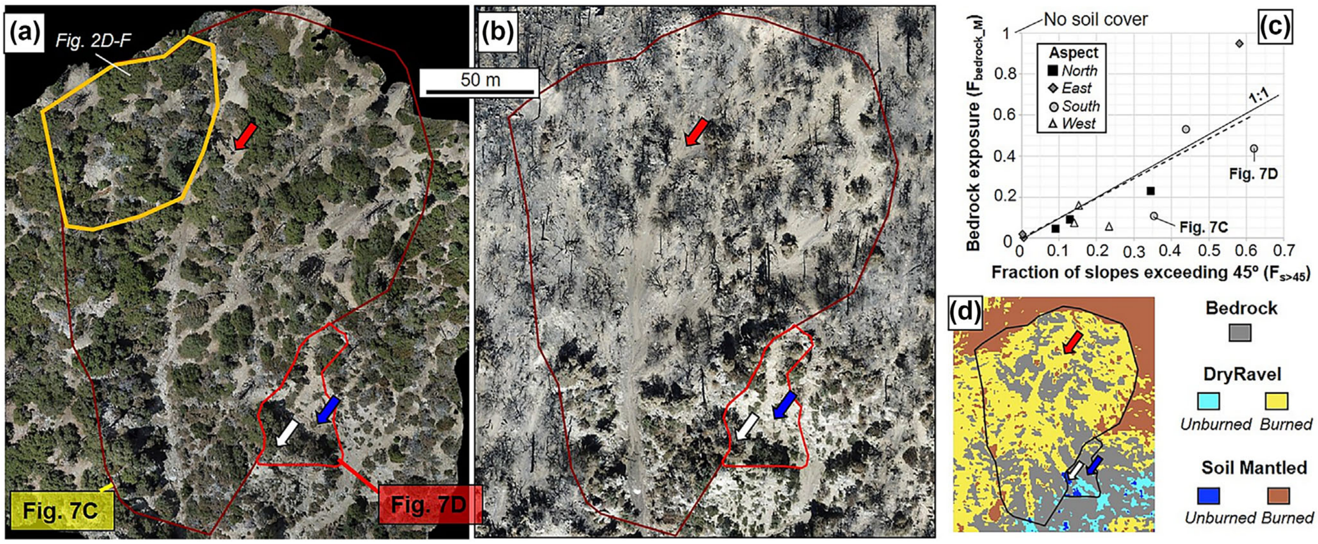

FIGURE 4 Ford Canyon mainstem (dark red polygon) and Ford Canyon tributary (smaller red polygon) sites prior to the fire in (a) September 2018 and following the fire in (b) November 2020. (c) Scaling relationship between fraction of local slopes exceeding 45° ($F_{S>45}$) and fraction of hillslopes with exposed bare bedrock mapped ($F_{bedrock\_M}$) for 12 calibration sites. Symbols correspond to main hillslope aspect. Dashed line indicates the best-fit least-squares linear regression pinned to the origin (0,0) and fit to all points, and solid line shows 1:1 relationship. (d) Inset shows the classification of hillslope sediment sources based on local slope and soil burn severity. Arrows link common positions between Figure 4a, 4b and 4d for a bare-bedrock slope (blue), a burned dry-ravel prone soil-mantled slope (red), and an unburned soil-mantled slope (white).

burn severities, and $A_{bedrock}$ represents the area of slopes exceeding the threshold gradient of 45° (Figure 3a, b). Moderate to high soil burn severity is typically associated with combustion of some roots and most surface fuels, which is needed to release sediment from debris wedges behind vegetation (DiBiase & Lamb, 2013; Parsons et al., 2010). We did not exclude any bedrock hillslopes (hillslopes with local slope angles > 45°) from mapping as a sediment source. Sediments are presumably unstable on these local slopes, but we found that bare-bedrock slopes were typically classified as unburned in satellite-derived burn maps because of limited vegetation cover. We assume that sediments on all soil-mantled slopes ($S < 45°$) with unburned or low soil-burn severity are stable. Sediment fluxes from recently burned slopes typically exceed long-term sediment fluxes contributed during unburned conditions by factors of 4–100 (e.g. East et al., 2021; Jackson & Roering, 2009; Lamb et al., 2011), suggesting that the contribution of sediment from unburned slopes is minimal over immediate postfire timescales.

The fractional extent for each hillslope sediment source is defined relative to the hillslope source area, A_{source}:

$$F_{soil} = \frac{A_{S<35}}{A_{source}} \quad (3)$$

$$F_{bedrock} = \frac{A_{S>45}}{A_{source}} \quad (4)$$

$$F_{ravel} = 1 - F_{soil} - F_{bedrock} \quad (5)$$

Together, the slopes comprising A_{source} represent the areas within the hillslope source region where loose sediment is most readily supplied to channels prior to and following the fire. For all mixing model cases, we assume that sediment delivery to channels from each hillslope source scales with areal exposure (i.e. spatially uniform erosion rate). For unburned conditions, we assume that sediment is only contributed to channels from bedrock cliff sources that have minimal hillslope sediment storage capacity. For burned hillslope conditions, we assume that sediment is delivered to channels from bare-bedrock slopes and burned soil-mantled slopes either immediately following the fire by dry ravel on steeper dry-ravel prone slopes between 35° and 45° (DiBiase & Lamb, 2020; Florsheim et al., 1991) or during precipitation events that drive soil erosion through rilling or gullying on soil-mantled slopes less than 35° (Alessio et al., 2021; Guilinger et al., 2020; Staley et al., 2014). These assumptions represent a reference scenario where sediment is produced at a uniform rate from all three sediment sources; however, sediments produced on soil-mantled slopes are only delivered to the channel when hillslopes are burned, whereas sediments supplied from bare-bedrock slopes are continuously delivered to channels.

3.2 | Quantification of sediment grain size distributions from hillslope sources and within channels

We used a combination of field sieving and grid-by-number point counts on scaled imagery to measure the wide range of sediment sizes across headwater channels and hillslope sediment sources (Table 2, supplementary dataset S2). To estimate sample size controls on grain size statistic uncertainty, we either used uncertainty estimates based on sample mass for sieving surveys or a subsampling technique for grid-by-number point counts (Marshall & Sklar, 2012; Rice & Church, 1996). The subsampling technique randomly resamples the total sediment grain size distribution of all clasts measured on scaled orthoimagery ($N = 1293$) using a sliding scale of subsample sizes that

TABLE 2 Sediment grain size surveys and bedrock fracture spacing measurement sites.

Name	Date	Method/location	Latitude (°)	Longitude (°)	Drainage area (m^2)	Sample size (*N* clasts or weight)[a]	D_{min} (cm)[b]	D_{50} (cm)	D_{84} (cm)	D_{95} (cm)
Mill creek 1 upstream	Aug. 2018	Photo Channel	34.0833	−116.9797	27,000	77	1	<1.0	1.7 ± 0.4	3.1 ± 1.2
Mill creek 1 downstream	Sept. 2018	SfM channel	34.0907	−116.9817	7,000	72	5	24.0 ± 5.9	40.9 ± 12.2	63.2 ± 28.1
Mill creek 2	Sept. 2018	SfM channel	34.0762	−116.9379	110,000	463	5	15.9 ± 1.3	48.1 ± 4.6	87.0 ± 9.1
Ford canyon mainstem	Sept. 2018	SfM channel	34.0636	−116.9340	18,000	142	5	32.3 ± 5.2	99.0 ± 19.6	300.0 ± 80.3
Mill creek 3	Sept. 2018	SfM channel	34.0836	−116.9538	89,000	631	5	22.9 ± 1.5	55.6 ± 4.4	92.3 ± 7.5
Ford canyon tributary	Sept. 2018	SfM channel	34.0639	−116.9334	1,000	99	5	16.5 ± 5.8	36.2 ± 9.0	55.4 ± 19.4
Wilson canyon mainstem	Aug. 2018	SfM channel	34.0831	−116.9831	4,000	119	5	15.0 ± 2.8	40.9 ± 9.2	68.4 ± 20.7
Wilson canyon cliffs	Aug. 2018	SfM channel	34.0830	−116.9831	1,000	87	5	5.9 ± 1.3	24.5 ± 6.6	46.9 ± 18.3
Mill creek 1 upstream	Aug. 2021	Sieve channel	34.0833	−116.9797	27,000	3.7 kg	0.025	0.1–0.2 (0.12)	0.8–1.6 (1.08)	1.6–3.2 (2.41)
Mill creek 1 upstream	Nov. 2020	Photo channel	34.0833	−116.9797	27,000	158	0.025	0.29 ± 0.04	1.36 ± 0.26	2.45 ± 0.58
Mill creek 1 downstream	Nov. 2020	SfM channel	34.0833	−116.9797	7,000	62	5	<5	34.2 ± 11.3	52.7 ± 27.5
Ford canyon mainstem	Nov. 2020	SfM channel	34.0636	−116.9340	18,000	182	5	<5	33.5 ± 5.8	158.6 ± 34.8
Ford canyon tributary	Nov. 2020	SfM channel	34.0636	−116.9340	1,000	100	5	13.5 ± 2.7	39.4 ± 9.7	59.0 ± 20.6
Wilson canyon mainstem	Nov. 2020	SfM channel	34.0831	−116.9831	4,000	140	5	8.0 ± 1.4	29.8 ± 6.3	58.0 ± 15.6
Wilson canyon cliffs	Nov. 2020	SfM channel	34.0830	−116.9831	1,000	107	5	8.3 ± 1.7	30.9 ± 7.4	53.3 ± 17.8
Mill creek 1 soil	Dec. 2021	Sieve hillslope	34.0836	−116.9820	-	4.6 kg	0.25	0.1–0.2 (0.15)	0.8–1.6 (0.88)	1.6–3.2 (2.72)
Soil photos	Nov. 2020	Photo hillslope	34.0836	−116.9820	-	623	1.6	<1.6	<1.6	5.5
Wilson dry ravel	Dec. 2021	Sieve hillslope	34.0828	−116.9819	-	6.2 kg	0.25	0.1–0.2 (0.14)	0.4–0.8 (0.53)	1.6–3.2 (1.71)

(Continues)

TABLE 2 (Continued)

Name	Date	Method/location	Latitude (°)	Longitude (°)	Drainage area (m^2)	Sample size (N clasts or weight)[a]	D_{min} (cm)[b]	D_{50} (cm)	D_{84} (cm)	D_{95} (cm)
Dry ravel photos	Nov. 2020	Photo hillslope	34.0828	−116.9819	-	389	1.6	<1.6	<1.6	<1.6
Wilshire cliff	Nov. 2020	SfM hillslope	34.0618	−116.9286	-	149	5	50.4	236.2	342.8
Ford cliff	Nov. 2020	SfM hillslope	34.0631	−116.9361	-	109	5	34.1	86.3	128.4
Wilson cliff spire	Aug. 2018	SfM hillslope	34.0815	−116.9856	-	285	5	99.0	202.2	374.1
Wilson cliff tributary	Nov. 2020	SfM hillslope	34.0829	−116.9833	-	124	5	21.5	59.2	101.8

[a] Number of grains in survey or total sediment mass sieved (kg). The 95% confidence intervals are calculated according to Section 3.2 for resolved D_{50}, D_{84} and D_{95} percentiles in grid-by-number photo surveys. Ranges bounded between sieve opening sizes are reported for sieve surveys, with percentile values estimated by log-transformed interpolation between sieve opening sizes in parentheses underneath (Bunte & Abt, 2001).

[b] Minimum sediment size resolved by measurement technique.

covers the smallest ($N = 62$) and largest ($N = 463$) number of grains counted in an individual survey. We calculated the absolute value of the difference among the D_{50}, D_{84}, and D_{95} size classes of the subsample and the total distribution, and we repeated this procedure 10,000 times. For each subsample size, we recorded the 95th percentile difference among the true D_{50}, D_{84}, and D_{95} of the total distribution and the D_{50}, D_{84}, and D_{95} estimated from the subsampled distribution. To calculate uncertainties at the 95% confidence interval as a direct function of sample size, we fit a negative power law function that approximates the decrease in percent error with increasing sample size for D_{50}, D_{84} and D_{95} size classes (Figure S2). This approach does not distinguish between different upper and lower 95% confidence interval bounds, which can differ if the total grain size distribution is skewed. These bounds likely represent a maximum range, because the total sediment grain size distribution was specifically collected to span a range of topographic and hillslope surface cover conditions seen across the landscape (i.e. Figure 2).

Our study addresses a null hypothesis that sediment grain size distributions are the same between surveys taken in the same locations before and after the fire. We use two approaches to test this hypothesis at sites where the median grain size is resolved in at least one of the repeat surveys. First, we assess whether the median grain size between the two repeat surveys differs by a factor larger than the two 95% confidence intervals surrounding the median grain size of each sample calculated from the subsampling approach. Second, a Mann–Whitney–Wilcoxon rank-sum significant difference test was used to detect change between repeat surveys of the same channel reach before and after the fire. This test considers a null hypothesis that individual measurements randomly selected from each sample have an equal probability of being higher or lower than one another if the two samples have the same underlying distribution. The test makes no assumptions about the underlying distribution shape and can compare samples with different numbers of individual measurements. To quantify the size of differences between the medians of repeat surveys, we calculate a Hodges–Lehman estimator and associated 95% confidence interval. The Hodges–Lehman estimator is calculated as the median of all possible pairwise difference combinations between the measurements in the paired prefire and postfire grain size distributions. We set all counts of sediment sizes that were finer than the photo resolution limit equal to the photo resolution limit, so the Hodges-Lehman estimator represents a minimum effect. We use a modified critical p-value of 0.0083, which reflects a critical p-value of 0.05 and the increased chance of recording one false instance of surface sediment grain size change across a total of six sites investigated.

3.2.1 | Headwater channel sediments (prefire and postfire)

We determined the size distribution of surface sediment cover in headwater channels before and after the 2020 El Dorado Fire using scaled orthoimagery derived from UAV-based SfM models described in Section 3.1.1. Headwater channels are generally inaccessible and contain large boulders which are difficult to measure with pebble count or field-sieve surveys. We used a grid-by-number technique where a 1-m spaced grid is overlain over the orthophoto, and the short axis is measured for each clast laying underneath a grid intersection (Bunte & Abt, 2001; Neely & DiBiase, 2020). We ignore grid intersections corresponding to shadows, vegetation or obstructed regions of orthophotos. We set the minimum resolvable clast size, $D_{\min}$, as 5 cm for 1-cm resolution aerial imagery (~3–5 pixels). We included the fraction of grid intersections that are beneath the resolution limit in the full grain size distribution to calculate the relative abundance of sediment that is finer than the resolution limit of our photographs.

3.2.2 | Hillslope and dry ravel sediments (Postfire)

We conducted three field-sieving surveys across two small headwater watersheds, including one channel bed site, one dry ravel deposit site, and one site on a low-sloping soil-mantled hillside. All samples were collected by amalgamating subsamples that were dug to 10-cm depth and taken at a 1-m interval along a 50-m tape line. Samples were collected during dry conditions. Organic material such as charcoal was not separated from bulk sediment but was unlikely to affect mass fractions because of sparse occurrence and low density. Approximately 4–6 kg of material was sieved in each sample at 1-ϕ intervals from a stack of 0.25 mm (2ϕ) to 32 mm (-5ϕ) sieves, yielding approximately 5% uncertainty at a size class of 6.4 cm (Church, 1987). We report mass fraction as the percent mass of bulk material passing through each sieve opening (i.e. finer than). We use a log-transformed interpolation to calculate D_{16}, D_{50}, D_{84} and D_{95} statistics between percentiles that correspond to sieve opening sizes (Bunte & Abt, 2001).

To improve our resolution of coarse sediment fractions that are difficult to sample by field-sieve techniques, we performed grid-by-number counts with a grid spacing of 10 cm on scaled photographs of the soil and dry ravel deposit surfaces. The scaled photographs sample patches of the soil or ravel surface at areas of ~0.5 m^2. Seven individual patches were analysed on the dry ravel deposit for a total area of 3.6 m^2, and 22 individual patches were analysed across soil-mantled slopes, for a total survey area of 4.6 m^2. We set the resolution limit of the photographs to 16 mm (-4ϕ), which corresponds to coarse fractions that are less likely to be sampled by sieve surveys (Marshall & Sklar, 2012). For grains intersected that are larger than 16 mm, we measured the length of the short axis on the photograph to approximate the clast *b*-axis length (Bunte & Abt, 2001). We counted the remaining fraction of grid intersections where the sediment size is finer than 16 mm, which represents the aerial percentage of the hillslope surface finer than 16 mm.

Grain size distributions measured from sieving and photographic techniques are not directly comparable but provide an approximate comparison in sites where these techniques overlap. It is not possible to measure the *c*-axis length from surface photographs, meaning a geometric conversion is not possible from *b*-axis length to passing a square sieve opening size (Adams, 1979; Church, 1987). Additionally, the short axis of exposed surface clasts can be shorter than the true *b*-axis length if grains are tilted, imbricated or buried, which may be expected in soils or postfire sediment loading conditions that partially cover sediment grains. Yet, comparisons of grain size statistics between photograph measurements and field-based point counts of gravel streams typically have uncertainties that are within the bounds of variability expected based on the number of grains analysed (Mair et al., 2022).

3.2.3 | Cliff-derived sediments and bedrock fracture spacing (prefire and postfire)

To approximate the size of coarse sediments contributed from bedrock cliffs, we used photographs from a 300-mm telephoto zoom lens on a handheld Nikon D5500 camera to construct 3D models of bedrock cliffs at four sites throughout Yucaipa Ridge following the 2020 El Dorado fire. We characterised the bedrock fracture network according to the methods described in Neely and DiBiase (2020). Bedrock fractures were traced on 1-cm pixel^{-1} orthoimages extracted along planes parallel to the approximately 100–500 m^2 cliff faces. For each site, bedrock fractures were traced within multiple representative cliff-face regions that are unobscured by vegetation or shadows (Thiele et al., 2017). Fracture density is calculated between the area of each cliff-face region and the sum of trace lengths within the region (Dershowitz & Herda, 1992). The short axis between fractures approximates the size of blocks bounded by fractures that are larger than the truncation limit imposed by photo resolution, and block sizes were sampled using a grid-by-number method with a grid spacing of 2 m.

3.3 | Predicted sediment grain size distribution of postfire sediment supply

We combined the fractional areas and grain size distributions of the three different hillslope sediment source types (Equation 5) to produce a predicted size distribution for the total postfire sediment supply. Two postfire cases are considered. One case only considers sediment supply from bedrock cliffs and burned ravel-prone slopes and represents an immediate postfire condition. The second case represents a condition where runoff generates additional soil erosion and considers sediment supply from bedrock cliff, burned dry-ravel prone slopes, and burned low-sloping soil-mantled slopes. We assume a direct scaling between the fractional areal extent of each hillslope source and the volume of postfire sediment available from each hillslope source; however, weighting coefficients could be applied to each of the three sediment source terms if more precise ratios of sediment supply can be constrained (Alessio et al., 2021; Guilinger et al., 2020; Staley et al., 2014). In the absence of such constraints, we only demonstrate reference cases where sediment is equally contributed per unit area from each hillslope sediment source, and sediment is mixed equally in the channel.

A probability density function (PDF) and corresponding cumulative distribution function (CDF) were fit to the measured sediment size distributions over the size range '*d*' [L] from each of the three sediment source types (i = bedrock, dry ravel and soil) assuming log-normal distribution as follows:

$$PDF(d)i = \frac{e^{\left(-(\ln(d)-\mu)^2/2(\sigma)^2\right)}}{\left(d\sigma\sqrt{2\pi}\right)} \tag{6}$$

$$CDF(d)i = \int_{-\infty}^{d} \frac{e^{-(\ln(d)/\sigma)/2}}{2\pi} \tag{7}$$

where μ and σ represent the natural logarithms of the mean and standard deviation, respectively. Goodness of fit and fit parameters are reported in Table S2.

The distribution of all bedrock fracture spacings measured on each of the four cliffs is used for the sediment sources corresponding to bedrock hillslopes. Dry ravel and soil sediment size distributions are used for the sediment sources corresponding to steep, dry-ravel prone and low-sloping soil-mantled slopes, respectively. For these fits, mass percentiles corresponding to each sieve opening were converted to a total of 1000 discrete values. We choose '*d*' to range from 0.1 mm (silt) to 10 m (large boulder). The mixed sediment grain size distribution, $CDF(d)_{tot}$, considers the percentages of sediment supplied from different hillslope source types in a burned watershed. $CDF(d)_{tot}$ serves as a reference case that can be used to evaluate connectivity between hillslopes and channels following the wildfire and the mixing of sediment from different hillslope sources. We consider the two cases of postfire sediment delivery described earlier in the texts:

$$CDF(d)_{tot\_r} = CDF(d)_{bedrock} F_{bedrock} / (F_{ravel} + F_{bedrock}) + CDF(d)_{ravel} F_{ravel} / (F_{bedrock} + F_{ravel}) \tag{8}$$

$$CDF(d)_{tot\_rs} = \mathrm{CDF(d)}_{bedrock} F_{bedrock} + CDF(d)_{ravel} F_{ravel} + CDF(d)_{s} F_{soil} \tag{9}$$

$CDF(d)_{tot\_r}$ represents an immediate postfire reference case, where sediments on low-sloping soil-mantled slopes remain stable. $CDF(d)_{tot\_rs}$ represents a case where runoff-driven erosion of low-sloping soil-mantled hillslopes delivers additional sediment.

3.4 | Estimated volumes of sediment delivered by dry ravel

We empirically constrained a vertical thickness of dry ravel contribution per unit area at eight field sites where hillslope length and dry ravel source area systematically increased from 36 to 140 m^2 moving along a forest road (Figure 3c). We calculated eight deposit volumes using the average of four measurements of dry ravel deposit thickness, four measurements of dry ravel deposit length measured parallel to the deposit slope and a 10-m wide deposit interval. Dry ravel deposit thickness was measured perpendicular from the deposit surface to the bottom of the burn layer, which consisted of abundant charcoal and fire-scarred clasts (Figure 3c, inset).

We fit a least-squares linear regression fixed through the origin between the eight dry ravel source areas and deposit volumes and calculate a best-fit vertical dry ravel yield of 4.4 cm (Figure S1B). This estimate is about half that of a longer-term average estimate of ~9.75 ± 0.25 cm of total vertical sediment supply, which can be derived from a time since the last fire of ~125 years (Minnich et al., 1995), catchment averaged erosion rates of 0.60 ± 0.17 mm yr^{-1} inferred from ^{10}Be concentrations of river sediment that integrate over 100–1000-year timescales (Argueta et al., 2023), and a rock to regolith density conversion factor of 1.3. In the absence of additional constraints, we assume that the empirically derived vertical thickness of 4.4 cm is representative of sediment contribution from dry-ravel prone hillslopes, although considerable variability in dry ravel response could occur between sites with different topography, hillslope sediment production, and vegetation density (DiBiase & Lamb, 2013, 2020; Lamb et al., 2011). For each headwater channel site, we calculate the vertical thickness of postfire dry ravel accumulation in the channel (H_{ravel}) (m) as

$$H_{ravel} = 0.044 \frac{A_{source} F_{ravel}}{A_{channel}} \tag{10}$$

where $A_{channel}$ is the area of the channel network mapped on digital orthophotos (Table 1) and typically corresponds to the extent of the surface sediment grain size survey site. This calculation assumes all dry ravel sediment reaches the channel and is equally distributed across the channel surface, meaning it is a maximum estimate of resurfacing thickness. We calculated uncertainty in ravel yield per unit area using conservative 90% confidence intervals surrounding the regression between source area and ravel volume (0.3–8.9 cm) and assume no additional uncertainty is contributed by A_{source} and $A_{channel}$.

4 | RESULTS

4.1 | Topography, soil cover, and bare-bedrock exposure across burned region

Across the study site, hillslopes steepen with the increasing exposure of bare-bedrock cliffs (Figure 4c). Mean hillslope gradients range from 25° to 50°, and soil cover ranges from a continuous soil mantle to 95% exposure of bare-bedrock cliffs (Table 1). The six sites with repeat sediment grain size surveys range from completely soil mantled, with most local slopes less than 35° ($F_{soil} \sim 1$) (Mill Creek 1 upstream); a patchwork of lower-sloping soil-mantled slopes, steeper dry ravel slopes, and bare-bedrock slopes (Mill Creek 1 downstream, Ford Canyon mainstem, and Wilson canyon mainstem); and mostly local slopes exceeding 45° ($F_{bedrock} \sim 1$) (Wilson Canyon tributary). A steep tributary of Ford canyon (Ford Canyon tributary) also displayed a patchwork of lower-sloping soil-mantled slopes, steeper dry ravel slopes and bare-bedrock slopes; however, this site experienced lower soil burn severities (Figure 4a, b and Table 1). There is no clear relationship between hillslope aspect, soil cover and soil burn severity at the scale of the surveyed watersheds (Figure S3). However, the south side of Yucaipa Ridge was burned at higher severity overall than the north-facing side of the ridge (Figure 1b).

4.2 | Sediments from hillslope source types: cliffs, ravel deposits and soils

Between four different cliffs, the D_{50} fracture spacing varies from 20 to 99 cm, D_{16} from 11 to 41 cm, and D_{84} from 60 to 210 cm (Figure 5). Between ~100 m long cliff complexes, the density of fractures with apertures approximately 1-cm wide or greater varies from a minimum of 1.65 m m^{-2} to a maximum fracture density of 4.90 m m^{-2}. The combined bedrock fracture density of all cliff faces measured is 2.00 m m^{-2}. The combined distribution of fracture spacings on all bedrock cliffs surveyed shows a median (D_{50}) fracture spacing of 59 cm (D_{16}, 21 cm; D_{84}, 154 cm; and D_{95}, 277 cm) (Figure 5).

The size distribution of soil and dry ravel sediments is 2–3 orders of magnitude finer than the size distribution of fracture bound blocks

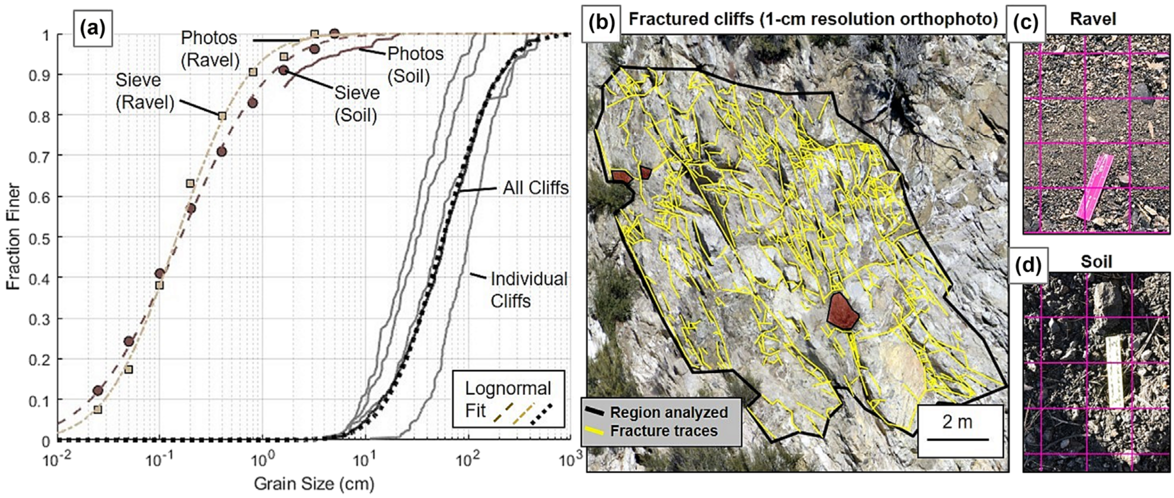

FIGURE 5 (a) Grain size distributions of different sediment source materials (i.e. bedrock cliff fracture spacing, dry ravel, and in-place soil). Brown circles and tan squares represent mass-fraction distributions from sieving bulk soil and dry ravel samples, respectively. Brown and tan curves represent distributions of particles with a short axis >1.6 cm on grid-to-number point counts on scaled photographs of soil and dry ravel deposit surfaces, respectively (c, d). Grey curves show bedrock fracture spacing distributions measured at individual cliff sites. Dashed curves show log-normal distribution fits to sediment grain size distributions of ravel, soil and all bedrock fracture spacing measurements on cliffs (black curve). (b) Mapped fracture traces (yellow) within representative cliff face patch (black outline) excluding vegetation (red shading) on 1-cm resolution cliff-face-normal orthophoto of cliffs in Ford Canyon. See Table S2 for fit statistics corresponding to the characteristic grain size distributions from each sediment source.

estimated from bedrock fracture spacings on exposed cliff faces. The D_{50} of soil is between 0.1 and 0.2 cm (interpolated estimate: 0.14 cm, Table 2), with D_{16} between 0.025 and 0.05 cm (interpolated estimate: 0.032 cm), and D_{84} of 0.8 to 1.6 cm (interpolated estimate: 0.87 cm). These estimates generally agree with the grid-by-number counts on scaled photographs of the soil surface, where ~15% of the grid-intersection clasts were coarser than 1.6 cm (Figure 5a). The grid-by-number counts of the soil-surface photographs capture the coarser tail of the sediment grain size distribution, including the largest but most infrequent soil-derived clasts with *b*-axes of ~20 cm.

The median sediment size of dry ravel is also between 0.1 and 0.2 cm (interpolated estimate: 0.13 cm); however, only 6% of the dry ravel by mass is coarser than 1.6 cm. This generally agrees with the grid-by-number counts on scaled photographs of the dry ravel surface, where 4% of the clasts intersected by the grid are coarser than 1.6 cm. The largest dry ravel clast sampled has a *b*-axis of 8.7 cm (Figure 5a). Silt and clay sized materials finer than 0.25 mm account for approximately 8–12% of the dry ravel and soil mass.

4.3 | Headwater channel sites

4.3.1 | Prefire locations with continuous hillslope soil cover

At the Mill Creek 1 upstream site, where hillslope sources are continuously soil-mantled with low hillslope gradients (Figure 2a–c), approximately 70% of the channel surface was covered by sediment sizes that are below the minimum size of resolvable grains given the photo resolution, prior to the 2020 El Dorado fire. The D_{50} grain size was finer than 1 cm (D_{84}, 1.6 cm; D_{95}, 3.0 cm; D_{100}, 9.2 cm). Generally, these grain size statistics reflect the size distribution of sediment measured on the soil-mantled hillslope site (Mill Creek 1 soil, Table 2) that is directly upstream from this channel location (D_{50}, 0.1–0.2 cm; D_{16}, 0.025–0.05 cm; D_{84}, 0.8–1.6 cm; D_{95}, 1.6–3.2 cm; and D_{100}, 21 cm).

4.3.2 | Prefire locations with bedrock cliffs exposed

Once bedrock is exposed on steep hillslopes (Figure 2d–i), size fractions of sediment in headwater channels coarsen and reflect bedrock fracture spacing distributions, generally scaled by a factor of 0.25–0.5 (Figures 6 and S4–S11). D_{50}, D_{84}, and D_{95} sediment sizes increase to 6–30, 31–98, and 54–300 cm, respectively. However, as more bare-bedrock slopes are exposed on hillslope sources, the size of D_{50}, D_{84} and D_{95} sediments does not systematically increase (grey boxes in Figure 6); instead, these sediment sizes continue to reflect the fracture spacing of bedrock cliffs (Neely & DiBiase, 2020). Boulders with intermediate axes of ~1 m are also present in each of the channels that have bedrock cliffs exposed in the source region, whereas these clasts were absent in the site with only soil-mantled source hillslopes (Figure 6c).

4.3.3 | Postfire changes in headwater channel sediment size

At the Mill Creek 1 upstream site with continuously soil-mantled hillslope sources and no bare bedrock exposed, the distribution of resolvable sediment sizes shows minimal change when comparing prefire and postfire channel sediment grain size surveys (Figure 7a). D_{84} sediment sizes do not differ considerably between prefire and postfire surveys (~1.6 cm). When the prefire D_{50} sediment size is extracted from a lognormal distribution fit to a left-censored distribution for sediment sizes below 1 cm, prefire D_{50} sediment size is 0.6 cm, approximately 2 times coarser than postfire sediment size

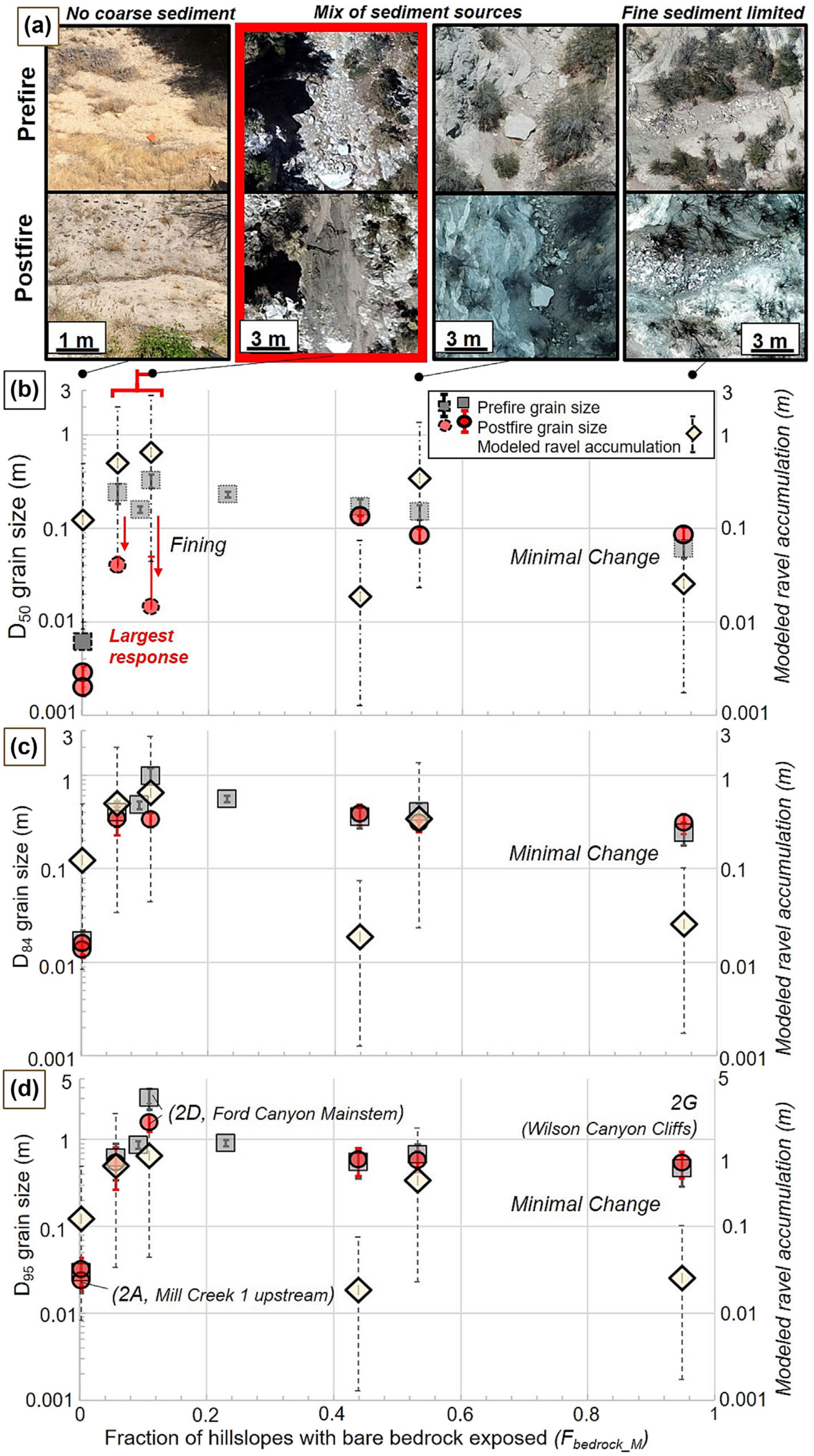

FIGURE 6 (a) Repeat images of channels before and after the fire. (b–d) Headwater channel surface sediment grain size statistics (B: D_{50}, C: D_{84}, D: D_{95}) plotted prior to the fire (2018) and immediately following the fire (2020) as a function of increasing the amount of bedrock exposed on hillslope sources ($F_{bedrock\_M}$, Equation 1). For sediment sizes that are below the photo resolution limit (dashed-outlined symbols), D_{50} is extracted from a lognormal distribution fit to left-censored distributions, and upper error bounds are fixed at the photo resolution limit. Diamonds indicate estimated vertical thickness of dry ravel accumulation at sites with repeat photo coverage based on Equation (10) (right vertical axis). The 90% confidence intervals are shown in dashed error bars.

(0.2–0.3 cm). A maximum possible change can be estimated from the minimum resolvable clast size of the prefire survey (~1 cm, 70th percentile) to the postfire D_{50} sediment size of 0.2–0.3 cm, meaning a maximum possible change in the D_{50} sediment size is 0.7–0.8 cm. The postfire sediment sizes measured in the channel that can be resolved (D_{50}, 0.2–0.3 cm; D_{16}, 0.05 cm; D_{84}, 1.3–1.6 cm; D_{95}, 2.4–3.2 cm; D_{100}, 29 cm) closely reflect the soil sediment grain size measured on the upstream hillslope (D_{50}, 0.2 cm; D_{16}, 0.05 cm; D_{84}, 0.8 cm; D_{95}, 3.2 cm; and D_{100}, 21 cm) (Figure 7).

Changes in channel sediment grain size show a dynamic response at sites where hillslope sources consist of a patchwork of soil-mantled and bare-bedrock slopes (red circles in Figure 6; Figure 7b, c). Bed sediment size decreases most significantly where bedrock was exposed on 6% and 11% of the contributing hillslopes at the Mill

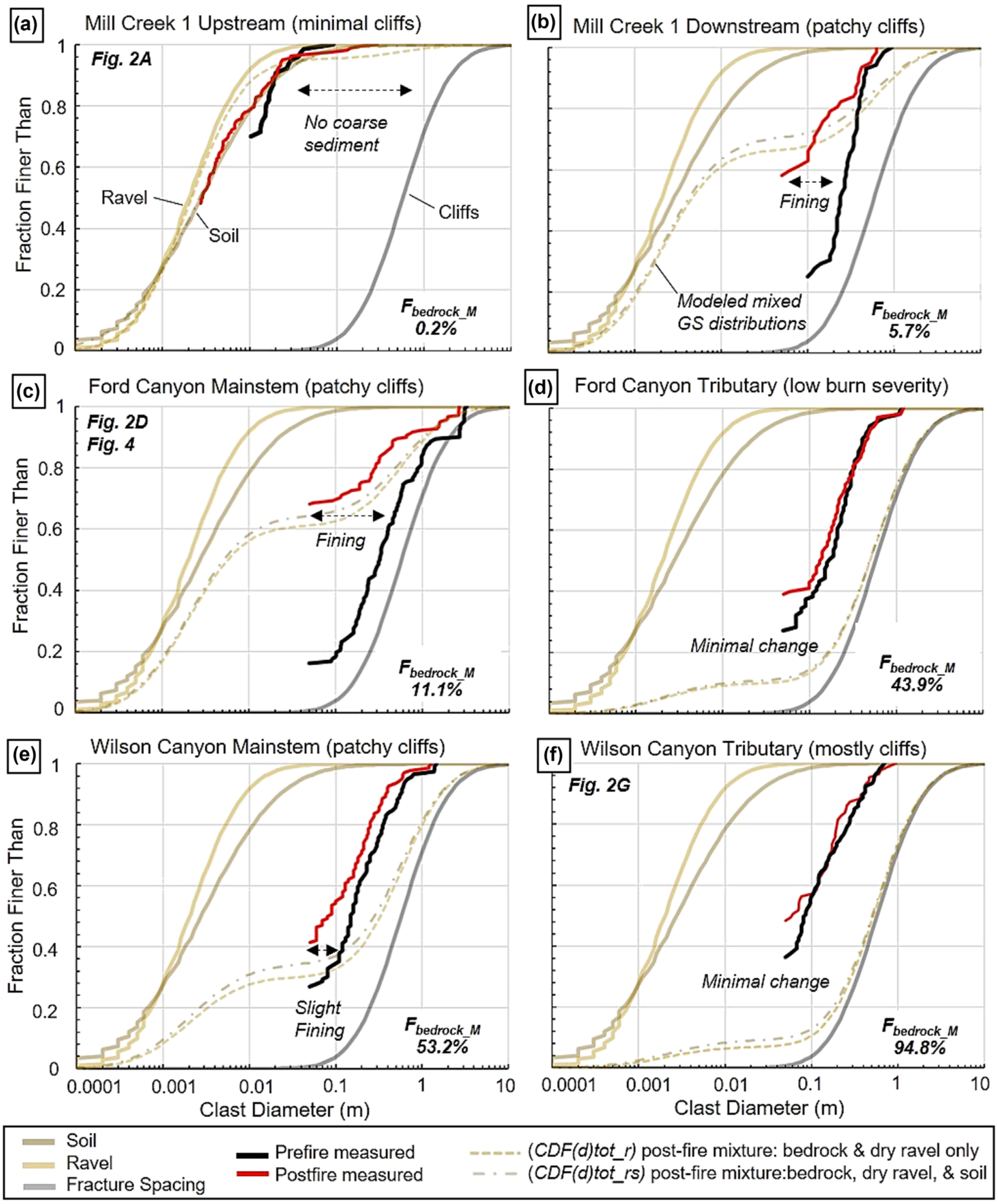

FIGURE 7 Comparison among prefire channel surface grain size (black), postfire channel surface grain size (red), sediment size distributions at different hillslope sources (soil, brown; ravel, tan; cliffs, grey), and sediment size distributions estimated according to equal mixing of sediment sources following the fire (dry ravel and bedrock only, Equation (8); and all sediment sources, Equation (9)). $F_{bedrock\_M}$ is coverted to a percent and increases from continuous (a) soil cover to a (b–e) patchwork of cliffs and soil cover, and nearly complete exposure of (f) bedrock cliffs.

Creek 1 downstream and Ford Canyon mainstem sites. The Mill Creek 1 site recorded a Mann–Whitney–Wilcoxon rank-sum *p*-value of 1.3×10^{-5} and a Hodges–Lehmann estimator of 15 cm with a 95% confidence interval from 6 to 18 cm. The Ford canyon mainstem site recorded a Mann–Whitney–Wilcoxon rank-sum *p*-value of 3.9×10^{-17} and a Hodges–Lehmann estimator of 18 cm with a 95% confidence interval from 13.2 to 24 cm. These Hodges–Lehmann estimators represent minimum estimates of the median of all possible pairwise differences between prefire and postfire *b*-axis measurement combinations, because postfire median grain sizes were finer than photo resolution limits in these two sites.

At these sites, the D_{50} grain size decreased from 24 and 32 cm before the fire to finer than the photo resolution limit of 5 cm after the fire. Considering a lognormal distribution fit to a left-censored distribution for sediment sizes below 5 cm (Bantis, 2024), postfire D_{50} grain size is approximately 4 cm at the Mill Creek 1 downstream site and 1.5 cm at the Ford Canyon site. This represents a minimum fining factor of 4.8 and 6.4 following the fire and an estimated factor of 6 and 21 when assuming lognormal grain size distributions for the sediment sizes below the resolution threshold of 5 cm. Both changes are larger than the 95% confidence interval surrounding the D_{50} grain size statistic in both sites (Figure 6a). Prefire versus postfire differences in the D_{84} and D_{95} sediment sizes are smaller and do not exceed sampling uncertainties of coarse sediment (Figure 6b, c).

Sites with high (>40%) bare-bedrock exposure showed a variable response, with no clear trend in sediment fining following the fire (Figure 7d–f). The D_{50} bed sediment size fined slightly following the fire at the Wilson Canyon mainstem site with bedrock exposure across 53% of source hillslopes (Mann–Whitney–Wilcoxon rank-sum *p*-value, 0.004; Hodges–Lehmann estimator of 5 cm with a 95% confidence interval from 0 to 10 cm); however, the median bed sediment size remained similar at the Ford Canyon tributary site (44% bedrock hillslopes), (Mann–Whitney–Wilcoxon rank-sum *p*-value, 0.22; Hodges–Lehmann estimator of 0 cm with a 95% confidence interval from 0 to 4 cm) and coarsened slightly at the Wilson Canyon tributary site (95% bedrock hillslopes) (Mann–Whitney-Wilcoxon rank-sum *p*-value, 0.23; Hodges–Lehmann estimator of 0 cm with a 95% confidence interval from -2 to 0 cm). At each of these three sites, the change in grain size following the fire was less than the sampling uncertainty of the prefire D_{50} sediment grain size (Figure 6a).

4.3.4 | Patterns of channel bed resurfacing by dry ravel

Postfire D_{50} channel-surface grain size is significantly finer than prefire conditions only in localities where cliffs are present and primarily where the estimated vertical thickness of dry ravel accumulation exceeds D_{50} grain size (Figure 6). In all sites with some fraction of bare-bedrock cliffs exposed in the source area, the estimated vertical thickness of dry ravel accumulation is smaller than the prefire D_{84} and D_{95} grain sizes of surface sediment cover. In addition, D_{84} and D_{95} grain size statistics change minimally before and after the fire (Figures 6 and 7). Changes in the grain size of channel surface cover surrounding fire appear consistent with potential volumes of dry ravel supply using a simplified scenario of dry ravel delivery from hillslopes to channels (Equation 10). However, this framework assumes that (1) our field surveys are representative of dry ravel processes across a wider region; (2) all dry ravel sediments are effectively delivered to the channel; (3) dry ravel is uniformly dispersed across the channel bed; and (4) comparison is possible between *b*-axis clast sizes and vertical ravel accumulation, which is presumably in the *c*-axis dimension.

5 | DISCUSSION

At a first order, our results imply that wildfires change the grain size distribution of surface sediment cover in headwater channels, particularly in catchments that have a mix of bare-bedrock and soil-mantled hillslope sources. Over the span of 2 years between the repeat surveys, headwater channels experienced (1) no change, (2) supply of sediments with the same grain size distribution as existing surface sediments, or (3) supply of sediment that is coarser or finer than the channel bed surface. Two out of six repeat surveys showed changes in median grain size that exceed the modified *p*-value and the sampling uncertainty at the 95% confidence interval (Figure 6), with the strongest effects observed in Ford Canyon ($p = 3.9 \times 10^{-17}$) and Mill Creek 1 downstream ($p = 1.3 \times 10^{-5}$) sites. It is challenging to negate the possibility that these changes in sediment grain size arise from sediment transport that was unrelated to fire during the 2-year interval between repeat surveys. However, rainfall intensities remained below debris-flow initiation thresholds over this time. In addition, minimal change in surface sediment grain size between 2018 and 2020 was observed at the Ford Canyon Tributary site, where soil burn severities were low (Figures S8 and S12).

Orthoimages from the Mill Creek 1 downstream postfire site and Wilson Canyon mainstem prefire site contain areas of distortion, overexposure, and warping, which effectively reduce the resolution of the UAV imagery (Figures S5–S10). These effects can obscure clast boundaries, which can result in clasts that are mapped as a collection of ‘fines’ that are below the resolution limit or a single large clast that actually represents a collection of smaller clasts with poorly resolved edges (Mair et al., 2022). We reason that this effect would increase the spread of the grain size distribution but is unlikely to drive our observed fining of grain sizes changes in grain size distributions. Our data show that the coarsest percentiles of the grain size distributions are similar between repeat surveys, and clast boundaries across 30–50% of the channel bed would have to be systematically obscured to generate the degree of postfire surface fining seen at the Mill Creek 1 downstream site (Figure 7).

Our repeat surveys demonstrate that the most dynamic postfire response in surface sediment grain size occurs in headwater channels where hillslope sources are a patchwork of bare-bedrock cliffs and soil-mantled hillslopes. We interpret that the patchwork of hillslope sources provides (1) coarse sediment derived from bedrock cliffs prior to fire and (2) significant volumes of finer sediment from soil-mantled slopes following the fire, in addition to minor fine sediment contributions sourced from fire spallation of cliffs. In the following sections, we discuss differences in sediment size between different hillslope sediment source types distinguished by threshold slopes and limitations to this approach (Section 5.1), differences in connectivity between different hillslope sediment source types and headwater channels implied by observed postfire changes in bed sediment grain size (Section 5.2), connections among topography, distinct sediment sources, and postfire debris flows (Section 5.3), and interactions among changing climates, wildfire dynamics, and the grain size distribution of sediment supplied to postfire debris flows (Section 5.4).

5.1 | The grain size of sediment supplied from hillslope sources distinguished by local slope

Our study design allows us to examine sediment supplied from soil-mantled and bare-bedrock hillslopes sources in isolation, which revealed stark differences in the grain size distributions supplied from these sediment sources. We also showed that the extent of these different sediment sources can be mapped using topographic slope thresholds. Yet, we are limited to an empirical approach that uses field measurements to describe sediment size distributions shed from each hillslope source type, because mechanistic connections among weathering process, inherited bedrock lithology, and sediment size remain challenging to interpret (Sklar et al., 2017, 2020; Wall et al., 2023).

Our field surveys show similar median grain sizes between in-place soils on low-gradient hillslopes and postfire dry ravel sourced from steeper soil-mantled slopes; however, hillslope soils contain a wider dispersion than dry ravel deposits. Both contain median grain sizes between 0.1 and 0.2 cm, which is similar to dry ravel sediment sizes from neighbouring crystalline ranges in the San Gabriel Mountains (Palucis et al., 2021), perhaps reflecting the fraction of crystalline bedrock that has been weathered and grussified.

The sampled sediment contributions from soil-mantled hillslopes are 2–4 orders of magnitude finer than the spacing between traced fractures on bedrock cliffs (Figure 5) and 1–2 orders of magnitude finer than the prefire grain size distribution of surface sediment cover in headwater channels where 5–95% of the hillslope sediment sources are exposed bare-bedrock (Figure 6). Compared to soil-mantled hillslopes, the near-surface weathering zone is presumably thinner and less active across bare-bedrock hillslopes, leading to the production of coarser material that has experienced less near-surface fragmentation (Román-Sánchez et al., 2021). If hillslopes approach or exceed frictional stability limits for loose material, coarse sediment is also transported to headwater channels prior to significant fining during hillslope sediment transport (e.g. Glade et al., 2017; Sklar et al., 2020). Although coarser than soil grain size distributions, surface sediment grain sizes in channels are 2–4 times finer than bedrock fracture spacing (Neely & DiBiase, 2020), which may reflect breakage of clasts during rockfall transport (Marc et al., 2021), detachment along near-surface fractures that form during the detachment process or are thinner than the resolution limits of the photographs (Berkowitz & Hadad, 1997; Eppes & Keanini, 2017), or geometric discrepancies between clast *b*-axis measurements (Church, 1987).

Two topographic slope thresholds broadly distinguish hillslope sediment source types by postfire response (in-place soils vs. dry-ravel prone soils) and presence or absence of soil (bare-bedrock cliffs); however, this approach may be more complicated when extending to landscapes with a wider variety of hillslope source terrains than what is observed across Yucaipa Ridge. The effectiveness of this hillslope sediment source classification on Yucaipa Ridge is primarily supported by the correspondence between fine sediment loading in headwater channels and the predicted supply of fine sediment from hillslope sediment sources partitioned by topography (Figure 6). Hillslope sediment transport processes are simplified in this framework, such that all dry ravel sediment reaches headwater channels, and sediment is uniformly spread across the channel bed surface. Additionally, calibration of local slope thresholds could vary depending on soil particle size, shape, or sorting; vegetation cohesion and density; or differences in point cloud filtering between lidar datasets (Lamb et al., 2013; Milodowski et al., 2015; Schmidt et al., 2001). These factors are likely minimised across Yucaipa Ridge, where bedrock units are pervasively fractured crystalline rocks (Allen, 1957; Bortugno & Spittler, 1986) and crystalline rocks are likely prone to grussification along mineral grains to produce a relatively narrow grain size distribution that is centred around sand-sized fractions (Figure 5). Using two threshold slopes to distinguish three sediment source types may overly simplify burned landscapes that span significant variations in underlying bedrock lithology (Alessio et al., 2021) or gradients in rock weathering related to local climate, elevation, hillslope aspect, or vegetation cover (Riebe et al., 2015); however, mixing models in these scenarios could consider a larger diversity of sediment sources.

5.2 | Wildfire controls on the delivery of sediment from hillslope sources to headwater channels

Our analysis compares surface sediment cover in headwater channels and a mixing model that considers sediment size distributions supplied from different hillslope sediment sources, weighted by the areal abundance of each sediment source type (Figure 7). This mixing scenario reflects a case where (1) our empirical measurements of sediment grain size accurately reflect the grain size distribution of sediment supplied from each hillslope sediment source; (2) each hillslope sediment source is eroding at the same rate; and (3) sediment delivered from each sediment source reaches the channel. We assume that these conditions are valid for the small spatial scales encompassed by each of the six small headwater catchments (e.g. drainage areas <0.1 km^2). In larger watersheds, this framework could also be used as a reference scenario comparing the grain size distribution of hillslope sediment supply to grain size distributions measured at different positions within the channel network.

Compared to the reference scenario, prefire surface sediment cover in headwater channels is coarser than expected by the mixing model, reflecting preferential sediment inputs from bare-bedrock cliffs (Figure 7b–f). Across the five sites with exposed bare bedrock cliffs, the fraction of bare-bedrock hillslope sources varies from 5% to 95%. However, the decreasing abundance of soil-mantled hillslopes is not reflected in the grain size of surface sediment cover across these headwater channels (Figure 6). Instead, channel surface sediment grain size distributions decouple from the grain size distribution of the total sediment flux from hillslopes to channels (Neely & DiBiase, 2020; Sklar et al., 2020), which presumably coarsens with increasing exposure of bare-bedrock cliffs (Attal et al., 2015; Sklar et al., 2020). We suggest that decoupling could result from a combination of (1) preferential storage of finer-grained material behind vegetation (Florsheim et al., 1991) and (2) development of armor layers in steep headwater channels as coarse sediment is supplied from bedrock cliffs (Parker & Sutherland, 1990).

Following the fire, the pattern of D_{50} fining in headwater channels illustrates that preferential storage of fine-grained material behind hillslope vegetation at least partially accounts for decoupling between the grain size distribution of hillslope sediment flux and that of the channel surface. Coarse prefire sediment cover in headwater channels is only buried in localities where the vertical thickness of estimated dry ravel supply exceeds the depth of coarse sediment sizes (Figure 6). Additionally, postfire surface sediment cover in each of the six headwater channels agrees with the mixing model predictions, which assume that sediment is equally delivered to the channel from an amount proportional to the areal extent of each hillslope sediment source (Figure 7). We are unable to constrain the magnitude of selective transport (winnowing) or burial of fine-grained material within channels without constraints on the grain size of the total sediment flux; however, our results show that storage of fine sediment on hillslopes behind vegetation partially controls coarsening of headwater channel surfaces prior to fires.

This result is consistent with field experiments and corresponding hillslope sediment transport models that route the trajectory of individual grains through either dry ravel or rockfall processes (DiBiase et al., 2017; Li & Lan, 2015; Roth et al., 2020). Runout distances are greatest for coarser sediment released from higher relief terrain, such as bedrock cliffs, because of increases in the ratio of clast diameter to hillslope roughness elements and initial particle velocity. Changes in headwater channel sediment grain size following fire imply feedbacks between hillslope vegetation cover and hillslope sediment flux for different grain size fractions that are supplied from weathering rock.

Despite significant postfire sediment accumulation, the grain size of surface sediment cover may change minimally in localities where the grain size of postfire sediment supply does not differ from the grain size of sediment on the channel surface prior to the fire (Figure 7a, f). In the site with no bare-bedrock cliff exposure in the hillslope source region (Mill Creek 1 Upstream), prefire D_{50}, D_{84} and D_{95} grain sizes are all exceeded by the estimated vertical thickness of dry ravel accumulation. However, no clear change is seen in the grain size of surface sediment cover between prefire and postfire surface sediment grain size (Figure 6). Here, the grain size of prefire surface sediment cover in the channel is similar to grain size distributions from soil and dry ravel sediment sources, which contribute to postfire sediment loading. Likewise, prefire and postfire surface sediment grain sizes may be similar despite significant sediment accumulation in headwater catchments dominated by bare-bedrock cliff sources only. Repeat imagery from the Wilson Canyon tributary site ($F_{\mathrm{bedrock\_m}} = 0.948$) indicates postfire delivery of rockfall sediment to the channel (Figures 6a and S10); however, more precise surveys of elevation change are required to quantify these changes in deposit volume (e.g. DiBiase & Lamb, 2020; Guilinger et al., 2020; Rengers et al., 2021). The surface sediment grain size distribution coarsens slightly at the Wilson Canyon tributary site following the fire (Figure 7). It is often difficult to discern between dry-ravel sediment released from behind burned vegetation and sediment supplied directly from fire spallation on cliff faces (Graber & Santi, 2023; Sarro et al., 2021), but postfire sediment added to the Wilson Canyon tributary site could be attributed directly to fire spallation and postfire rockfall processes, because of the scarcity of prefire hillslope vegetation at this site.

5.3 | Sediment supply from soil-mantled and bare-bedrock hillslopes and postfire debris flows

We hypothesise that the postfire fining response is maximised in steep landscapes that display a patchwork of soil-mantled and bare-bedrock hillslope sources, and that this patchwork is common throughout actively-uplifting, steep mountain ranges (Benjaram et al., 2022; DiBiase et al., 2012; Milodowski et al., 2015; Neely et al., 2019). On Yucaipa Ridge, the patchwork of steep dry-ravel prone hillslopes and bare-bedrock cliffs is pervasive (Figure 1), likely related to rapid rock uplift rates and landsliding (Binnie et al., 2007). The end-member sites that we chose which are continuously soil mantled or 95% bare-bedrock hillslopes are limited to small headwater regions (drainage areas <0.1 km^2). Larger watersheds integrate a mixture of hillslope sediment sources.

Conceptually, this patchwork develops as channel incision rates increase to balance rock uplift rates, and hillslopes steepen towards the stability angles of soil and rock (Burbank et al., 1996; DiBiase et al., 2023; Neely et al., 2019; Schmidt & Montgomery, 1995). In such settings, coarse sediment bypasses the hillslope weathering zone and can directly enter colluvial channels through landslides or rockfalls (Marc et al., 2021; Neely & DiBiase, 2020; Roda-Boluda et al., 2018). On steep hillslopes, sediment travel distances also increase with increasing particle size, leading to downslope coarsening and a higher likelihood of coarse sediment reaching headwater channel deposits (DiBiase et al., 2017; Neely & DiBiase, 2020; Roth et al., 2020). Compared to topography with gentle soil-mantled hillslopes, the transition to steeper threshold hillslopes represents a condition where sediment fluxes are high, a mixture of coarse and fine sediment sources exists in the watershed, and the volume and grain size of sediment stored at different positions throughout a watershed depends strongly on the presence or absence of hillslope vegetation (Figure 7).

The combined mixture of sediment contributed from bedrock cliffs and burned soil-mantled slopes can elevate debris-flow hazards in multiple ways. First, our sampling suggests that sediment coarser than cobbles likely comes from prefire sediment contributed from bedrock cliffs and landslides, because of the low abundance of these size fractions in soil and dry ravel (Figure 5). Reduction of surface sediment grain size following fire lowers entrainment thresholds of sediment in steep channels (McGuire et al., 2017; Palucis et al., 2021). Additionally, debris-flow volumes are commonly elevated in regions with significant dry ravel response (DiBiase & Lamb, 2020), and fine sediment supply can be even more substantial if rilling mobilises soils from gentler hillslopes (Alessio et al., 2021; Guilinger et al., 2020; Staley et al., 2014). Importantly, even if in low abundance, coarse prefire sediment contributed from bedrock cliffs often concentrates into debris-flow fronts, which can govern local flow speeds, heights, and runout distances (e.g. Zanuttigh & Lamberti, 2007; Jones et al., 2023).

Calibration between topographic data, sediment sources, and the grain size of sediment supply in the context of the fire cycle offers an approach to estimate the mixed grain size distribution of sediments that are available following the fire (Equations 9 and 10). This approach may be useful to constrain sediment inputs to debris-flow runout scenarios at the scale of small watersheds that pose postfire debris-flow hazards (e.g. Barnhart et al., 2021). However, it is limited by (1) requiring empirical field measurements, (2) the accuracy of the calibration between topographic data and sediment source type (Figures 4 and 5), and (3) uncertainty constraining catchment-scale sediment budgets with respect to the fire cycle (DiBiase & Lamb, 2013). Additionally, local variability in hillslope topography, soil cover, aspect, and sediment storage between headwater catchments may decouple the conditions at debris-flow nucleation points from the characteristics of hillslopes across an entire source watershed (DiBiase & Lamb, 2020; Neely et al., 2019; Rengers et al., 2016). The downstream position of debris-flow initiation points has been shown to control initial debris-flow volumes and the likelihood that a debris flow will propagate downstream (Barnhart et al., 2021), but this position also sets the spatial scale of hillslope sources that are integrated to produce the grain size distribution of sediment supply, which varied across the six headwater catchments that were the focus of this study (Figure 6).

As a first attempt, we calculated grain size distributions using a mixing model that considers the extent of two watersheds that produced destructive debris flows during Tropical Storm Kay in September 2022 (Figures 8 and S12). News reports containing eyewitness accounts and video footage showed debris flows on both the north and south sides of Yucaipa Ridge, and these flows carried boulder-sized sediment (Arreola, 2022; Gabriel, 2022; Petri & Yee, 2022). Photographs and videos from these events indicate qualitative differences in debris-flow runouts that correspond to differences in burn severity and the predicted grain size of sediments supplied from hillslope sources on the south and north side of Yucaipa

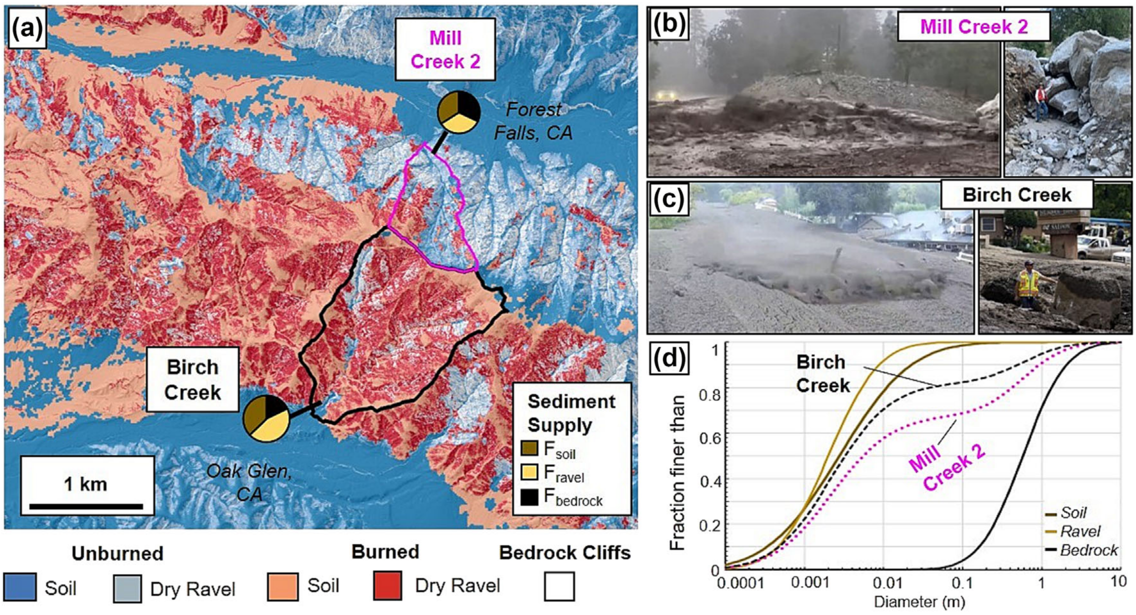

FIGURE 8 Example mixed sediment size distributions from two watersheds that produced destructive debris flows during Tropical Storm Kay (September 2022). (a) Hillslope sediment sources classified by topography and soil burn severity. Pie charts show the proportion of postfire sediment availability from bare-bedrock (black), burned-dry-ravel (tan) and burned-soil-mantled (brown) hillslopes in the source area (Equations 2–5). 95% of Birch Creek and 48% of Mill Creek 2 were burned at moderate or high soil burn severities. (b and c, left) Still frames from videos of debris flows crossing outlets of (b) Mill Creek 2 and (c) Birch Creek and photographs of debris-flow deposits (right). (d) Empirically derived grain size distributions for bedrock fracture spacing (black), soil (brown), and dry ravel (tan), and predicted sediment size distributions supplied at the catchment scale for Mill Creek 2 and Birch Creek based on Equation (9). Photographs provided by Mike DeFrisco, California Geological Survey (Figure 8b), Sanchez and Weber (2022), and county of San Bernardino public works (Figure 8c).

Ridge (Figure 8). Ground surveys of deposit grain size distributions were not measured and compared with hillslope sediment sources (e.g. Kean et al., 2019); however, these comparisons are possible in future events. This calculation assumes that full watershed extents are the relevant debris-flow source areas and that these flows were not initiated in individual tributaries that differed in their sediment supply conditions from the rest of the watershed.

5.4 | Interactions between changing climate and coarse prefire sediment in postfire settings

Our analysis on Yucaipa Ridge demonstrates the importance of mixing both postfire sediment supplied from burned soil-mantled slopes and coarse prefire colluvium that was delivered from bare-bedrock cliffs (Figures 7 and 8). Across other landscapes, prefire colluvial channel deposits can reflect sediment storage that accumulated over decadal to millennial timescales (e.g. Reneau et al., 1990) and considerably longer timescales in channel systems with abundant sediment supply from prior landslides (Li et al., 2016; Scherler et al., 2016) or landscape change related to deglaciation (Deng et al., 2017). Moreover, in two landscapes that were unaffected by recent wildfires in southern California, direct observations of sediment motion from repeat aerial photographs indicated that much of the coarsest colluvial channel sediment remained in place despite experiencing storms with decadal recurrence intervals (Neely & DiBiase, 2023). Landscape disturbances such as wildfire may be necessary to empty these sediment reservoirs. In the wake of shifting climate and wildfire regimes, sediment supply to debris flows remains uncertain (Hirschberg et al., 2021), and coarse sediment released from colluvial channels could amplify the largest postfire debris-flow events (Kean & Staley, 2021; Morell et al., 2021), particularly in regions that have not historically burned or show potential for higher severity wildfires as climates change (Abatzoglou et al., 2021; Gergel et al., 2017).

6 | CONCLUSIONS

We constrained the connection among hillslope morphology, bedrock cliff exposure, and the size of sediments delivered to headwater channels prior to and immediately following the 2020 El Dorado fire, which burned steep terrain on Yucaipa Ridge in the San Bernardino Mountains, California. Following the wildfire, change in the grain size of sediment supplied from hillslope sources has been invoked as one of the precursors to postfire debris flows. We provide field data that document changes in the grain size of hillslope sediment supply with respect to the fire cycle, and we interpret processes responsible for these changes in a landscape that is characteristic of many steep, debris-flow-prone mountain ranges of southern California.

We characterised the size distribution of sediments contributed from three different hillslope source types, which are distinguished by slope thresholds that delineate hillslope response to fire: low-sloping soil-mantled hillslopes with local slopes less than 35°, where soil cover remains in place after burning; soil-mantled hillslopes steeper than 35° where sediment is released as dry ravel following the fire; and bare-bedrock cliffs which are typically steeper than 45° and do not sustain soil cover. Sediment sizes measured on low-sloping soil-mantled slopes and dry-ravel prone slopes are generally similar (D_{50} of

0.1–0.2 cm), but 2–4 orders of magnitude finer than particle sizes estimated from bedrock fracture spacings on cliffs.

Both prior to and following the wildfire, we compared the size distribution of sediments supplied from these hillslope source types to the size distribution of sediments in six headwater channels where hillslope sediment sources vary from fully soil mantled, to a patchwork of soil cover and bare bedrock, and to fully bare-bedrock cliffs. Prior to wildfire, the surface sediment grain size of steep headwater channels reflected sediment inputs from bedrock cliffs, regardless of whether cliff exposure was 5–95% of the hillslope source region. For fully soil-mantled catchments, sediment size in headwater channels is finer and reflects sediment inputs from soil-mantled slopes where weathering has reduced the size of sediments. Following the wildfire, the delivery of fine sediment from soil-mantled and dry-ravel hillslopes can lead to the resurfacing of headwater channels and grain size reduction, because of the incineration of vegetation dams on hillslopes that preferentially store fine sediment between fires. We found that postfire reduction in channel sediment grain size is largest in channels that have some bare bedrock cliffs (5–11%) but are mostly soil mantled. Repeat surveys constrain a 5- to 20-fold reduction in surface D_{50} sediment size in these catchments. The surface sediment grain size in fully soil-mantled catchments remains similar to prefire soil grain size distributions, and the lack of fine sediment storage in bedrock-dominated catchments between fires limits the potential for grain size fining in headwater channels.

Across the steep topography examined, hillslopes that consist of a patchwork of soil-mantled and bare-bedrock slopes at the watershed scale show the most dynamic changes in channel sediment grain size following the fire. The mixture of coarse sediment supplied from bedrock cliffs and fine sediment supplied by burned soil-mantled slopes may amplify postfire debris-flow hazards downstream. We used a combination of topographic proxies that classify hillslope sediment sources and direct measurements that constrain the grain size of sediment supplied from these sediment sources to upscale predictions of postfire sediment grain size to the scale of small debris-flow-prone watersheds. Although empirical and limited by the complex nature of rock weathering across various lithologic, climatic, and tectonic settings, this approach can serve as a reference case to compare to postfire debris-flow deposits and may aid in characterising the grain size distribution of sediment supply prior to impending postfire debris-flow hazards.

AUTHOR CONTRIBUTIONS

Alexander B. Neely, Leonard S. Sklar, Seulgi Moon and Roman A. DiBiase conceptualised the project. Funding was acquired by Seulgi Moon and Roman A. DiBiase. Methods were developed by Alexander B. Neely and supported by Seulgi Moon, Roman A. DiBiase, Marina O. Argueta and Leonard S. Sklar as the project evolved. Alexander B. Neely led data collection efforts and was assisted by Marina O. Argueta. Computational analysis was conducted by Alexander B. Neely. Alexander B. Neely was supervised by Roman A. DiBiase during the period of data collection and Seulgi Moon and Leonard S. Sklar during the period of data analysis. Alexander B. Neely wrote the initial draft. Alexander B. Neely led efforts to discuss research with private landowners and state agencies. Seulgi Moon, Roman A. DiBiase, Marina O. Argueta, Leonard S. Sklar and Alexander B. Neely revised and edited subsequent drafts together.

ACKNOWLEDGEMENTS

This work was supported by the National Science Foundation grants EAR-1945431 and EAR-2012073 awarded to S. Moon and grants EAR-1848321 and EAR-1608014 awarded to R. DiBiase. The authors would like to thank Doug Choudy, Jason Laird, David Herrero, and Frazier Haney of the Bearpaw Reserve, and Connie Clark of Pilgrim Pines Camp for sharing observations, experiences, and allowing a portion of this research to take place on their property during a time of continued distress. We thank Christian Erikson, Julia Carr, Justin Higa, and Xuesong Ding for their assistance in the field and discussion throughout the preparation of this manuscript. Discussions with Daniel Boateng, Alex Beer, and Christoph Glotzbach at the University of Tübingen and Brian Swanson, Don Lindsay, Kirk Townsend, Paul Burgess, and Alex Morelan at the California Geological Survey provided additional feedback on results and interpretations. The authors would also like to thank four anonymous reviewers and the editing staff at ESPL for constructive feedback and suggestions. Open Access funding enabled and organized by Projekt DEAL.

DATA AVAILABILITY STATEMENT

UAV-derived imagery used for bedrock exposure mapping, analysis of bedrock fracture spacing, and sediment grain size measurements are hosted on opentopography.com (https://doi.org/10.5069/G9028PRS, https://doi.org/10.5069/G9V9869B), along with USGS 3DEP program aerial lidar datasets used for topographic analysis. Supplementary dataset includes ArcGIS shapefiles showing extent of field surveys for bare bedrock exposure mapping (Figure 4) and sediment grain size distributions measured in channels (Figures 6 and 7). Supplementary dataset also includes a supporting information table containing detailed information on 3D structure-from-motion photogrammetry surveys.

ORCID

Alexander B. Neely https://orcid.org/0000-0001-6142-2627
Seulgi Moon https://orcid.org/0000-0001-5207-1781
Roman A. DiBiase https://orcid.org/0000-0002-5347-8396

REFERENCES

Abatzoglou, J.T., Rupp, D.E., O'Neill, L.W. & Sadegh, M. (2021) Compound extremes drive the western Oregon wildfires of September 2020. *Geophysical Research Letters*, 48(8), e2021GL092520. Available from: https://doi.org/10.1029/2021GL092520

Adams, J. (1979) Gravel size analysis from photographs. *Journal of the Hydraulics Division*, 105(10), 1247–1255. Available from: https://doi.org/10.1061/JYCEAJ.0005283

Adams, K.V., Dixon, J.L., Wilcox, A.C. & McWethy, D. (2023) Fire-produced coarse woody debris and its role in sediment storage on hillslopes. *Earth Surface Processes and Landforms*, 48(9), 1665–1678. Available from: https://doi.org/10.1002/esp.5573

Alessio, P., Dunne, T. & Morell, K. (2021) Post-wildfire generation of debris-flow slurry by rill erosion on colluvial hillslopes. *Journal of Geophysical Research - Earth Surface*, 126(11), e2021JF006108. Available from: https://doi.org/10.1029/2021JF006108

Allen, C.R. (1957) San Andreas fault zone in San Gorgonio pass, southern California. *Geological Society of America Bulletin*, 68(3), 315–350. Available from: https://doi.org/10.1130/0016-7606(1957)68[315:SAFZIS]2.0.CO;2

Argueta, M.O., Moon, S., Blisniuk, K., Brown, N.D., Corbett, L.B., Bierman, P.R., et al. (2023) Examining the influence of disequilibrium landscape on millennial-scale erosion rates in the San Bernardino

Mountains, California, USA. *GSA Bulletin*, 136(3–4), 1526–1540. Available from: https://doi.org/10.1130/B36734.1

Arreola, A. (2022) Homes and roads in mountain communities damaged by mudslides, debris flows. *NBC Los Angeles*. https://www.nbclosangeles.com/news/local/homes-and-roads-in-mountain-communities-damaged-by-mudslides-debris-flows/2983873/

Attal, M., Mudd, S.M., Hurst, M.D., Weinman, B., Yoo, K. & Naylor, M. (2015) Impact of change in erosion rate and landscape steepness on hillslope and fluvial sediments grain size in the Feather River basin (Sierra Nevada, California). *Earth Surface Dynamics*, 3(1), 201–222. Available from: https://doi.org/10.5194/esurf-3-201-2015

Barnhart, K.R., Jones, R.P., George, D.L., McArdell, B.W., Rengers, F.K., Staley, D.M., et al. (2021) Multi-model comparison of computed debris flow runout for the 9 January 2018 Montecito, California post-wildfire event. *Journal of Geophysical Research - Earth Surface*, 126(12), e2021JF006245. Available from: https://doi.org/10.1029/2021JF006245

Bantis, L. (2024). Fit distributions to censored data (https://www.mathworks.com/matlabcentral/fileexchange/38226-fit-distributions-to-censored-data), MATLAB Central File Exchange. Retrieved March 14, 2024.

Benjaram, S.S., Dixon, J.L. & Wilcox, A.C. (2022) Capturing the complexity of soil evolution: heterogeneities in rock cover and chemical weathering in Montana's Rocky Mountains. *Geomorphology*, 404, 108186. Available from: https://doi.org/10.1016/j.geomorph.2022.108186

Berkowitz, B. & Hadad, A. (1997) Fractal and multifractal measures of natural and synthetic fracture networks. *Journal of Geophysical Research - Solid Earth*, 102(B6), 12205–12218. Available from: https://doi.org/10.1029/97JB00304

Binnie, S.A., Phillips, W.M., Summerfield, M.A. & Fifield, L.K. (2007) Tectonic uplift, threshold hillslopes, and denudation rates in a developing mountain range. *Geology*, 35(8), 743–746. Available from: https://doi.org/10.1130/G23641A.1

Bortugno, E.J. & Spittler, T.E. (1986) *Geologic map of the San Bernardino quadrangle, California, map 3A (Geol.), scale 1: 250,000 edition*. Sacramento: Calif. Div. of Mines and Geol.

Bunte, K. & Abt, S.R. (2001) *Sampling surface and subsurface particle-size distributions in wadable gravel-and cobble-bed streams for analyses in sediment transport, hydraulics, and streambed monitoring*. Gen. Tech. Rep. RMRS-GTR-74. Fort Collins, CO: U.S. Department of Agriculture, Forest Service, Rocky Mountain Research Station 428 p.

Burbank, D.W., Leland, J., Fielding, E., Anderson, R.S., Brozovic, N., Reid, M.R., et al. (1996) Bedrock incision, rock uplift and threshold hillslopes in the northwestern Himalayas. *Nature*, 379(6565), 505–510. Available from: https://doi.org/10.1038/379505a0

Cannon, S.H., Gartner, J.E., Wilson, R.C., Bowers, J.C. & Laber, J.L. (2008) Storm rainfall conditions for floods and debris flows from recently burned areas in southwestern Colorado and southern California. *Geomorphology*, 96(3–4), 250–269. Available from: https://doi.org/10.1016/j.geomorph.2007.03.019

Church, M.A. (1987) River bed gravels: sampling and analysis. *Sediment Transport in Gravel-Bed Rivers*, 43–88.

De Graff, J.V. & Gallegos, A.J. (2012) The challenge of improving identification of rockfall hazard after wildfires. *Environmental & Engineering Geoscience*, 18(4), 389–397. Available from: https://doi.org/10.2113/gseegeosci.18.4.389

Deng, M., Chen, N. & Liu, M. (2017) Meteorological factors driving glacial till variation and the associated periglacial debris flows in Tianmo Valley, south-eastern Tibetan plateau. *Natural Hazards and Earth System Sciences*, 17(3), 345–356. Available from: https://doi.org/10.5194/nhess-17-345-2017

Dershowitz, W.S. & Herda, H.H. (1992) Interpretation of fracture spacing and intensity. In: *Paper presented at the 33rd U.S. symposium on rock mechanics (USRMS)*. Santa Fe, New Mexico.

DiBiase, R.A., Heimsath, A.M. & Whipple, K.X. (2012) Hillslope response to tectonic forcing in threshold landscapes. *Earth Surface Processes and Landforms*, 37(8), 855–865. Available from: https://doi.org/10.1002/esp.3205

DiBiase, R.A. & Lamb, M.P. (2013) Vegetation and wildfire controls on sediment yield in bedrock landscapes. *Geophysical Research Letters*, 40(6), 1093–1097. Available from: https://doi.org/10.1002/grl.50277

DiBiase, R.A. & Lamb, M.P. (2020) Dry sediment loading of headwater channels fuels post-wildfire debris flows in bedrock landscapes. *Geology*, 48(2), 189–193. Available from: https://doi.org/10.1130/G46847.1

DiBiase, R.A., Lamb, M.P., Ganti, V. & Booth, A.M. (2017) Slope, grain size, and roughness controls on dry sediment transport and storage on steep hillslopes. *Journal of Geophysical Research - Earth Surface*, 122(4), 941–960. Available from: https://doi.org/10.1002/2016JF003970

DiBiase, R.A., Neely, A.B., Whipple, K.X., Heimsath, A.M. & Niemi, N.A. (2023) Hillslope morphology drives variability of detrital 10Be erosion rates in steep landscapes. *Geophysical Research Letters*, 50(16), p.e2023GL104392. Available from: https://doi.org/10.1029/2023GL104392

East, A.E., Logan, J.B., Dartnell, P., Lieber-Kotz, O., Cavagnaro, D.B., McCoy, S.W., et al. (2021) Watershed sediment yield following the 2018 Carr fire, Whiskeytown national recreation area, northern California. *Earth and Space Science*, 8(9), p.e2021EA001828. Available from: https://doi.org/10.1029/2021EA001828

Eppes, M.C. & Keanini, R. (2017) Mechanical weathering and rock erosion by climate-dependent subcritical cracking. *Reviews of Geophysics*, 55(2), 470–508. Available from: https://doi.org/10.1002/2017RG000557

Florsheim, J.L., Chin, A., Kinoshita, A.M. & Nourbakhshbeidokhti, S. (2017) Effect of storms during drought on post-wildfire recovery of channel sediment dynamics and habitat in the southern California chaparral, USA. *Earth Surface Processes and Landforms*, 42(10), 1482–1492. Available from: https://doi.org/10.1002/esp.4117

Florsheim, J.L., Keller, E.A. & Best, D.W. (1991) Fluvial sediment transport in response to moderate storm flows following chaparral wildfire, Ventura County, southern California. *Geological Society of America Bulletin*, 103(4), 504–511. Available from: https://doi.org/10.1130/0016-7606(1991)103%3C0504:FSTIRT%3E2.3.CO;2

Foufoula-Georgiou, E., Ganti, V. & Dietrich, W.E. (2010) A nonlocal theory of sediment transport on hillslopes. *Journal of Geophysical Research - Earth Surface*, 115(F2). Available from: https://doi.org/10.1029/2009JF001280

Gabet, E.J. & Mendoza, M.K. (2012) Particle transport over rough hillslope surfaces by dry ravel: experiments and simulations with implications for nonlocal sediment flux. *Journal of Geophysical Research - Earth Surface*, 117(F1). Available from: https://doi.org/10.1029/2011JF002229

Gabriel, A. (2022) 'Rocks the size of recliners': mudslide fills Southern California steakhouse with up to 7 feet of debris. Fox. *Weather*. https://www.foxweather.com/extreme-weather/mudslide-debris-southern-california-steakhouse

Gergel, D.R., Nijssen, B., Abatzoglou, J.T., Lettenmaier, D.P. & Stumbaugh, M.R. (2017) Effects of climate change on snowpack and fire potential in the western USA. *Climatic Change*, 141(2), 287–299. Available from: https://doi.org/10.1007/s10584-017-1899-y

Glade, R.C., Anderson, R.S. & Tucker, G.E. (2017) Block-controlled hillslope form and persistence of topography in rocky landscapes. *Geology*, 45(4), 311–314. Available from: https://doi.org/10.1130/G38665.1

Graber, A. & Santi, P. (2023) UAV-photogrammetry rockfall monitoring of natural slopes in Glenwood canyon, CO, USA: background activity and post-wildfire impacts. *Landslides*, 20(2), 229–248. Available from: https://doi.org/10.1007/s10346-022-01974-9

Guilinger, J.J., Gray, A.B., Barth, N.C. & Fong, B.T. (2020) The evolution of sediment sources over a sequence of postfire sediment-laden flows revealed through repeat high-resolution change detection. *Journal of Geophysical Research - Earth Surface*, 125(10), e2020JF005527. Available from: https://doi.org/10.1029/2020JF005527

Heimsath, A.M., DiBiase, R.A. & Whipple, K.X. (2012) Soil production limits and the transition to bedrock-dominated landscapes. *Nature Geoscience*, 5(3), 210–214. Available from: https://doi.org/10.1038/NGEO1380

Hirschberg, J., Fatichi, S., Bennett, G.L., McArdell, B.W., Peleg, N., Lane, S.N., et al. (2021) Climate change impacts on sediment yield and debris-flow activity in an alpine catchment. *Journal of Geophysical Research - Earth Surface*, 126(1), p.e2020JF005739. Available from: https://doi.org/10.1029/2020JF005739

Huebl, J. & Kaitna, R. (2021) Monitoring debris-flow surges and triggering rainfall at the Lattenbach Creek, Austria. *Environmental & Engineering Geoscience*, 27(2), 213–220. Available from: https://doi.org/10.2113/EEG-D-20-00010

Hyde, K.D., Wilcox, A.C., Jencso, K. & Woods, S. (2014) Effects of vegetation disturbance by fire on channel initiation thresholds. *Geomorphology*, 214, 84–96. Available from: https://doi.org/10.1016/j.geomorph.2014.03.013

Jackson, M. & Roering, J.J. (2009) Post-fire geomorphic response in steep, forested landscapes: Oregon Coast Range, USA. *Quaternary Science Reviews*, 28(11–12), 1131–1146. Available from: https://doi.org/10.1016/j.quascirev.2008.05.003

Jones, R.P., Rengers, F.K., Barnhart, K.R., George, D.L., Staley, D.M. & Kean, J.W. (2023) Simulating debris flow and levee formation in the 2D shallow flow model D-claw: channelized and unconfined flow. *Earth and Space Science*, (2), e2022EA002590. Available from: https://doi.org/10.1029/2022EA002590

Kean, J.W. & Staley, D.M. (2021) Forecasting the frequency and magnitude of postfire debris flows across southern California. *Earth's Future*, 9(3), e2020EF001735. Available from: https://doi.org/10.1029/2020EF001735

Kean, J.W., Staley, D.M., Lancaster, J.T., Rengers, F.K., Swanson, B.J., Coe, J.A., et al. (2019) Inundation, flow dynamics, and damage in the 9 January 2018 Montecito debris-flow event, California, USA: opportunities and challenges for post-wildfire risk assessment. *Geosphere*, 15(4), 1140–1163. Available from: https://doi.org/10.1130/GES02048.1

Keeley, J.E. & Syphard, A.D. (2016) Climate change and future fire regimes: examples from California. *Geosciences*, 6(3), 37. Available from: https://doi.org/10.3390/geosciences6030037

Kostynick, R., Matinpour, H., Pradeep, S., Haber, S., Sauret, A., Meiburg, E., et al. (2022) Rheology of debris flow materials is controlled by the distance from jamming. *Proceedings of the National Academy of Sciences*, 119(44), e2209109119. Available from: https://doi.org/10.1073/pnas.2209109119

Lague, D., Brodu, N. & Leroux, J. (2013) Accurate 3D comparison of complex topography with terrestrial laser scanner: application to the Rangitikei canyon (NZ). *ISPRS Journal of Photogrammetry and Remote Sensing*, 82, 10–26. Available from: https://doi.org/10.1016/j.isprsjprs.2013.04.009

Lamb, M.P., Levina, M., DiBiase, R.A. & Fuller, B.M. (2013) Sediment storage by vegetation in steep bedrock landscapes: theory, experiments, and implications for postfire sediment yield. *Journal of Geophysical Research - Earth Surface*, 118(2), 1147–1160. Available from: https://doi.org/10.1002/jgrf.20058

Lamb, M.P., Scheingross, J.S., Amidon, W.H., Swanson, E. & Limaye, A. (2011) A model for fire-induced sediment yield by dry ravel in steep landscapes. *Journal of Geophysical Research - Earth Surface*, 116(F3), F03006. Available from: https://doi.org/10.1029/2010JF001878

Larsen, I.J., Pederson, J.L. & Schmidt, J.C. (2006) Geologic versus wildfire controls on hillslope processes and debris flow initiation in the Green River canyons of dinosaur National Monument. *Geomorphology*, 81(1–2), 114–127. Available from: https://doi.org/10.1016/j.geomorph.2006.04.002

Li, L. & Lan, H. (2015) Probabilistic modeling of rockfall trajectories: a review. *Bulletin of Engineering Geology and the Environment*, 74(4), 1163–1176. Available from: https://doi.org/10.1007/s10064-015-0718-9

Li, G., West, A.J., Densmore, A.L., Hammond, D.E., Jin, Z., Zhang, F., et al. (2016) Connectivity of earthquake-triggered landslides with the fluvial network: implications for landslide sediment transport after the 2008 Wenchuan earthquake. *Journal of Geophysical Research - Earth Surface*, 121(4), 703–724. Available from: https://doi.org/10.1002/2015JF003718

Lukens, C.E., Riebe, C.S., Sklar, L.S. & Shuster, D.L. (2016) Grain size bias in cosmogenic nuclide studies of stream sediment in steep terrain. *Journal of Geophysical Research - Earth Surface*, 121(5), 978–999. Available from: https://doi.org/10.1002/2016JF003859

Mair, D., Do Prado, A.H., Garefalakis, P., Lechmann, A., Whittaker, A. & Schlunegger, F. (2022) Grain size of fluvial gravel bars from close-range UAV imagery—uncertainty in segmentation-based data. *Earth Surface Dynamics*, 10(5), 953–973. Available from: https://doi.org/10.5194/esurf-10-953-2022

Marc, O., Turowski, J.M. & Meunier, P. (2021) Controls on the grain size distribution of landslides in Taiwan: the influence of drop height, scar depth and bedrock strength. *Earth Surface Dynamics*, 9(4), 995–1011. Available from: https://doi.org/10.5194/esurf-9-995-2021

Marshall, J.A. & Sklar, L.S. (2012) Mining soil databases for landscape-scale patterns in the abundance and size distribution of hillslope rock fragments. *Earth Surface Processes and Landforms*, 37(3), 287–300. Available from: https://doi.org/10.1002/esp.2241

McGuire, L.A., Kean, J.W., Staley, D.M., Rengers, F.K. & Wasklewicz, T.A. (2016) Constraining the relative importance of raindrop-and flow-driven sediment transport mechanisms in postwildfire environments and implications for recovery time scales. *Journal of Geophysical Research - Earth Surface*, 121(11), 2211–2237. Available from: https://doi.org/10.1002/2016JF003867

McGuire, L.A., Rengers, F.K., Kean, J.W. & Staley, D.M. (2017) Debris flow initiation by runoff in a recently burned basin: is grain-by-grain sediment bulking or en masse failure to blame? *Geophysical Research Letters*, 44(14), 7310–7319. Available from: https://doi.org/10.1002/2017GL074243

Meyer, G.A. & Wells, S.G. (1997) Fire-related sedimentation events on alluvial fans, Yellowstone National Park, USA. *Journal of Sedimentary Research*, 67(5), 776–791. Available from: https://doi.org/10.1306/D426863A-2B26-11D7-8648000102C1865D

Milodowski, D.T., Mudd, S.M. & Mitchard, E.T.A. (2015) Topographic roughness as a signature of the emergence of bedrock in eroding landscapes. *Earth Surface Dynamics*, 3(4), 483–499. Available from: https://doi.org/10.5194/esurf-3-483-2015

Minnich, R.A. (1986) Snow levels and amounts in the mountains of southern California. *Journal of Hydrology*, 89(1–2), 37–58. Available from: https://doi.org/10.1016/0022-1694(86)90141-1

Minnich, R.A. (1988) *The biogeography of fire in the San Bernardino Mountains of California: a historical study*, Vol. 28. Univ of California Press.

Minnich, R.A., Barbour, M.G., Burk, J.H. & Fernau, R.F. (1995) Sixty years of change in Californian conifer forests of the San Bernardino Mountains. *Conservation Biology*, 9(4), 902–914. Available from: https://doi.org/10.1046/j.1523-1739.1995.09040902.x

Moore, J.R., Sanders, J.W., Dietrich, W.E. & Glaser, S.D. (2009) Influence of rock mass strength on the erosion rate of alpine cliffs. *Earth Surface Processes and Landforms*, 34(10), 1339–1352. Available from: https://doi.org/10.1002/esp.1821

Morell, K.D., Alessio, P., Dunne, T. & Keller, E. (2021) Sediment recruitment and redistribution in Mountain Channel networks by post-wildfire debris flows. *Geophysical Research Letters*, 48(24), e2021GL095549. Available from: https://doi.org/10.1029/2021GL095549

Morton, D.M., Alvarez, R.M., Ruppert, K.R. & Goforth, B. (2008) Contrasting rainfall generated debris flows from adjacent watersheds at Forest Falls, southern California, USA. *Geomorphology*, 96(3–4), 322–338. Available from: https://doi.org/10.1016/j.geomorph.2007.03.021

Murphy, B.P., Czuba, J.A. & Belmont, P. (2019) Post-wildfire sediment cascades: a modeling framework linking debris flow generation and network-scale sediment routing. *Earth Surface Processes and Landforms*, 44(11), 2126–2140. Available from: https://doi.org/10.1002/esp.4635

Neely, A.B. & DiBiase, R.A. (2020) Drainage area, bedrock fracture spacing, and weathering controls on landscape-scale patterns in surface sediment grain size. *Journal of Geophysical Research - Earth Surface*, 125(10), e2020JF005560. Available from: https://doi.org/10.1029/2020JF005560

Neely, A.B. & DiBiase, R.A. (2023) Sediment controls on the transition from debris flow to fluvial channels in steep mountain ranges. *Earth*

Surface Processes and Landforms, 48(7), 1342–1361. Available from: https://doi.org/10.1002/esp.5553

Neely, A.B., DiBiase, R.A., Corbett, L.B., Bierman, P.R. & Caffee, M.W. (2019) Bedrock fracture density controls on hillslope erodibility in steep, rocky landscapes with patchy soil cover, southern California, USA. *Earth and Planetary Science Letters*, 522, 186–197. Available from: https://doi.org/10.1016/j.epsl.2019.06.011

Neely, A., DiBiase, R., Moon, S., Carr, J., Argueta, M. & Erikson, C. (2023a) UAV surveys of Yucaipa ridge, CA catchments after the 2020 El Dorado fire. Distributed by. *OpenTopography*. Available from: https://doi.org/10.5069/G9V9869B. Accessed: January 3, 2024.

Neely, A., DiBiase, R., Moon, S., Carr, J. & Erikson, C. (2023b) UAV surveys of Yucaipa ridge, CA, watersheds (2018) prior to El Dorado fire. Distributed by. *OpenTopography*. Available from: https://doi.org/10.5069/G9028PRS. Accessed: January 3, 2024.

Nyman, P., Box, W.A., Stout, J.C., Sheridan, G.J., Keesstra, S.D., Lane, P.N., et al. (2020) Debris-flow-dominated sediment transport through a channel network after wildfire. *Earth Surface Processes and Landforms*, 45(5), 1155–1167. Available from: https://doi.org/10.1002/esp.4785

Palucis, M.C., Ulizio, T.P. & Lamb, M.P. (2021) Debris flow initiation from ravel-filled channel bed failure following wildfire in a bedrock landscape with limited sediment supply. *Geological Society of America Bulletin*, 133(9–10), 2079–2096. Available from: https://doi.org/10.1130/B35822.1

Parker, G. & Sutherland, A.J. (1990) Fluvial armor. *Journal of Hydraulic Research*, 28(5), 529–544. Available from: https://doi.org/10.1080/00221689009499044

Parsons, A., Robichaud, P.R., Lewis, S.A., Napper, C. & Clark, J.T. (2010) *Field guide for mapping post-fire soil burn severity*, Vol. 243. Fort Collins, CO, USA: US Department of Agriculture, Forest Service, Rocky Mountain Research Station.

Petri, A. & Yee, G. (2022) Evacuation ordered ahead of possible mud, debris flows in San Bernardino County. *Los Angeles Times*. https://www.latimes.com/california/story/2022-09-12/flash-flood-southern-california-rain-mudslides-thunderstorms

Reneau, S.L., Dietrich, W.E., Donahue, D.J., Jull, A.T. & Rubin, M. (1990) Late Quaternary history of colluvial deposition and erosion in hollows, Central California Coast Ranges. *Geological Society of America Bulletin*, 102(7), 969–982. Available from: https://doi.org/10.1130/0016-7606(1990)102%3C0969:LQHOCD%3E2.3.CO;2

Rengers, F.K., McGuire, L.A., Coe, J.A., Kean, J.W., Baum, R.L., Staley, D.M., et al. (2016) The influence of vegetation on debris-flow initiation during extreme rainfall in the northern Colorado front range. *Geology*, 44(10), 823–826. Available from: https://doi.org/10.1130/G38096.1

Rengers, F.K., McGuire, L.A., Kean, J.W., Staley, D.M., Dobre, M., Robichaud, P.R., et al. (2021) Movement of sediment through a burned landscape: sediment volume observations and model comparisons in the San Gabriel Mountains, California, USA. *Journal of Geophysical Research - Earth Surface*, 126(7), p.e2020JF006053. Available from: https://doi.org/10.1029/2020JF006053

Rice, S. & Church, M. (1996) Sampling surficial fluvial gravels; the precision of size distribution percentile sediments. *Journal of Sedimentary Research*, 66(3), 654–665. Available from: https://doi.org/10.2110/jsr.66.654

Riebe, C.S., Sklar, L.S., Lukens, C.E. & Shuster, D.L. (2015) Climate and topography control the size and flux of sediment produced on steep mountain slopes. *Proceedings of the National Academy of Sciences*, 112(51), 15574–15579. Available from: https://doi.org/10.1073/pnas.1503567112

Roda-Boluda, D.C., D'Arcy, M., McDonald, J. & Whittaker, A.C. (2018) Lithological controls on hillslope sediment supply: insights from landslide activity and grain size distributions. *Earth Surface Processes and Landforms*, 43(5), 956–977. Available from: https://doi.org/10.1002/esp.4281

Roering, J.J. & Gerber, M. (2005) Fire and the evolution of steep, soil-mantled landscapes. *Geology*, 33(5), 349–352. Available from: https://doi.org/10.1130/G21260.1

Román-Sánchez, A., Temme, A., Willgoose, G., van den Berg, D., Gura, C.M. & Vanwalleghem, T. (2021) The fingerprints of weathering: grain size distribution changes along weathering sequences in different lithologies. *Geoderma*, 383, 114753. Available from: https://doi.org/10.1016/j.geoderma.2020.114753

Roth, D.L., Doane, T.H., Roering, J.J., Furbish, D.J. & Zettler-Mann, A. (2020) Particle motion on burned and vegetated hillslopes. *Proceedings of the National Academy of Sciences*, 117(41), 25335–25343. Available from: https://doi.org/10.1073/pnas.1922495117

Sanchez, M. & Weber, C. (2022) Southern California mudslides damage homes, carry away cars. *Apnews*, https://apnews.com/article/wildfires-storms-forests-los-angeles-california-ec4741740e63cc1821b926bd2342749f

Santi, P.M., Dewolfe, V.G., Higgins, J.D., Cannon, S.H. & Gartner, J.E. (2008) Sources of debris flow material in burned areas. *Geomorphology*, 96(3–4), 310–321. Available from: https://doi.org/10.1016/j.geomorph.2007.02.022

Sarro, R., Pérez-Rey, I., Tomás, R., Alejano, L.R., Hernández-Gutiérrez, L.E. & Mateos, R.M. (2021) Effects of wildfire on rockfall occurrence: a review through actual cases in Spain. *Applied Sciences*, 11(6), 2545. Available from: https://doi.org/10.3390/app11062545

Scherler, D., Lamb, M.P., Rhodes, E.J. & Avouac, J.P. (2016) Climate-change versus landslide origin of fill terraces in a rapidly eroding bedrock landscape: San Gabriel River, California. *Geological Society of America Bulletin*, 128(7–8), 1228–1248. Available from: https://doi.org/10.1130/B31356.1

Schmidt, K., Hanshaw, M., Howle, J., Kean, J., Staley, D., Stock, J., et al. (2011) Hydrologic conditions and terrestrial laser scanning of post-firedebris flows in the San Gabriel Mountains, CA, U.S.A. *Italian Journal of Engineering Geology and Environment*, 583–593. Available from: https://doi.org/10.4408/IJEGE.2011-03.B-064

Schmidt, K.M. & Montgomery, D.R. (1995) Limits to relief. *Science*, 270(5236), 617–620. Available from: https://doi.org/10.1126/science.270.5236.617

Schmidt, K.M., Roering, J.J., Stock, J.D., Dietrich, W.E., Montgomery, D.R. & Schaub, T. (2001) The variability of root cohesion as an influence on shallow landslide susceptibility in the Oregon Coast Range. *Canadian Geotechnical Journal*, 38(5), 995–1024. Available from: https://doi.org/10.1139/t01-031

Sklar, L.S., Riebe, C.S., Genetti, J., Leclere, S. & Lukens, C.E. (2020) Downvalley fining of hillslope sediment in an alpine catchment: implications for downstream fining of sediment flux in mountain rivers. *Earth Surface Processes and Landforms*, 45(8), 1828–1845. Available from: https://doi.org/10.1002/esp.4849

Sklar, L.S., Riebe, C.S., Marshall, J.A., Genetti, J., Leclere, S., Lukens, C.L., et al. (2017) The problem of predicting the size distribution of sediment supplied by hillslopes to rivers. *Geomorphology*, 277, 31–49. Available from: https://doi.org/10.1016/j.geomorph.2016.05.005

Spotila, J.A., Farley, K.A., Yule, J.D. & Reiners, P.W. (2001) Near-field transpressive deformation along the San Andreas fault zone in southern California, based on exhumation constrained by (U-Th)/He dating. *Journal of Geophysical Research - Solid Earth*, 106(B12), 30909–30922. Available from: https://doi.org/10.1029/2001JB000348

Staley, D.M., Negri, J.A., Kean, J.W., Laber, J.L., Tillery, A.C. & Youberg, A.M. (2017) Prediction of spatially explicit rainfall intensity–duration thresholds for post-fire debris-flow generation in the western United States. *Geomorphology*, 278, 149–162. Available from: https://doi.org/10.1016/j.geomorph.2016.10.019

Staley, D.M., Wasklewicz, T.A. & Kean, J.W. (2014) Characterizing the primary material sources and dominant erosional processes for post-fire debris-flow initiation in a headwater basin using multi-temporal terrestrial laser scanning data. *Geomorphology*, 214, 324–338. Available from: https://doi.org/10.1016/j.geomorph.2014.02.015

Steel, Z.L., Safford, H.D. & Viers, J.H. (2015) The fire frequency-severity relationship and the legacy of fire suppression in California forests. *Ecosphere*, 6(1), 1–23. Available from: https://doi.org/10.1890/ES14-00224.1

Terweh, S., Hassan, M.A., Mao, L., Schrott, L. & Hoffmann, T.O. (2021) Bio-climate affects hillslope and fluvial sediment grain size along the

Chilean Coastal Cordillera. *Geomorphology*, 384, 107700. Available from: https://doi.org/10.1016/j.geomorph.2021.107700

Thiele, S.T., Grose, L., Samsu, A., Micklethwaite, S., Vollgger, S.A. & Cruden, A.R. (2017) Rapid, semi-automatic fracture and contact mapping for point clouds, images and geophysical data. *Solid Earth*, 8(6), 1241–1253. Available from: https://doi.org/10.5194/se-8-1241-2017

U.S. Geological Survey. (2020) *USGS one meter CA SoCal wildfires B1 2018, United States Geological Survey 3D elevation program 1 meter digital elevation model*.

USDA Forest Service Burn Area Response Taskforce. (2020) *El Dorado 2020 Burned Area Report*. US Forest Service.

Wall, S., Murphy, B.P., Belmont, P. & Yocom, L. (2023) Predicting post-fire debris flow grain sizes and depositional volumes in the intermountain West, United States. *Earth Surface Processes and Landforms*, 48(1), 179–197. Available from: https://doi.org/10.1002/esp.5480

Writer, J.H. & Murphy, S.F. (2012) Wildfire effects on source-water quality—lessons from Fourmile canyon fire, Colorado, and implications for drinking-water treatment. *U.S. Geological Survey Fact Sheet*, 2012–3095, 4 p.

Zanuttigh, B. & Lamberti, A. (2007) Instability and surge development in debris flows. *Reviews of Geophysics*, 45(3). Available from: https://doi.org/10.1029/2005RG000175

SUPPORTING INFORMATION

Additional supporting information can be found online in the Supporting Information section at the end of this article.

How to cite this article: Neely, A.B., Moon, S., DiBiase, R.A., Sklar, L.S. & Argueta, M.O. (2024) The grain size of sediments delivered to steep debris-flow prone channels prior to and following wildfire. *Earth Surface Processes and Landforms*, 1–24. Available from: https://doi.org/10.1002/esp.5819